

Herschel Far-Infrared Photometry of the Swift Burst Alert Telescope Active Galactic Nuclei Sample of the Local Universe. I. PACS Observations¹

M. Meléndez; R. F. Mushotzky

and

T. T. Shimizu

Astronomy Department, University of Maryland, Stadium Dr. , College Park, MD, 20742,
USA

marcio@astro.umd.edu

A. J. Barger^{1,2}

Department of Astronomy, University of Wisconsin-Madison, 475 N. Charter Street,
Madison, WI 53706, USA

and

L. L. Cowie

Institute for Astronomy, University of Hawaii, 2680 Woodlawn Drive, Honolulu, HI 96822,
USA

Received _____; accepted _____

¹Department of Physics and Astronomy, University of Hawaii, 2505 Correa Road, Honolulu, HI 96822, USA

²Institute for Astronomy, University of Hawaii, 2680 Woodlawn Drive, Honolulu, HI 96822, USA

ABSTRACT

Far-Infrared (FIR) photometry from the the Photodetector Array Camera and Spectrometer (PACS) on the *Herschel* Space Observatory is presented for 313 nearby, hard X-ray selected galaxies from the 58-month *Swift* Burst Alert Telescope (BAT) Active Galactic catalog. The present data do not distinguish between the FIR luminosity distributions at 70 and 160 μm for Seyfert 1 and Seyfert 2 galaxies. This result suggests that if the FIR emission is from the nuclear obscuring material surrounding the accretion disk, then it emits isotropically, independent of orientation. Alternatively, a significant fraction of the 70 and 160 μm could be from star formation, independent of AGN type. Using a non-parametric test for partial correlation with censored data, we find a statistically significant correlation between the AGN intrinsic power (in the 14-195 keV band) and the FIR emission at 70 and 160 μm for Seyfert 1 galaxies. We find no correlation between the 14-195 keV and FIR luminosities in Seyfert 2 galaxies. The observed correlations suggest two possible scenarios: (i) if we assume that the FIR luminosity is a good tracer of star formation, then there is a connection between star formation and the AGN at sub-kiloparsec scales, or (ii) dust heated by the AGN has a statistically significant contribution to the FIR emission. Using a Spearman rank-order analysis, the 14-195 keV luminosities for the Seyfert 1 and 2 galaxies are weakly statistically correlated with the F_{70}/F_{160} ratios.

¹*Herschel* is an ESA space observatory with science instruments provided by European-led Principal Investigator consortia and with important participation from NASA.

1. Introduction

In the past few years there has been an incredible amount of information regarding the infrared view of our dusty Universe. With the advent of very successful space missions such as *Spitzer* (Werner et al. 2004), NASA’s *Wide-field Infrared Survey Explorer* (WISE, Wright et al. 2010), *AKARI* (Murakami et al. 2007), *Plank* (Planck Collaboration et al. 2011) and *Herschel* (Pilbratt et al. 2010), the mid-infrared (MIR) and far-infrared (FIR) is beginning to provide a unique perspective into the evolution of galaxies via dust-based star formation rate (SFR) indicators. However, these SFR indicators are not free from systematic uncertainties primarily due to the nature of dust in the galaxy by trapping the starlight and re-emitting (a fraction) in the infrared. Because of this, each MIR and FIR band can be associated with a different dust component, different spatial distributions and different stellar age populations (see Kennicutt & Evans 2012, for a review). For these reasons, monochromatic infrared emission may be restricted, as a reliable SFR indicator, to large samples of galaxies for statistically significant studies (e.g., Calzetti et al. 2010). On the other hand, SFR indicators that rely on the total FIR emission are subject to uncertainties because they are very susceptible to the shape of the MIR to FIR spectral energy distribution (e.g., Kennicutt 1998). Despite these considerations and given the plethora of new and more sensitive infrared surveys, these SFR metrics are widely used. However, little consideration is given to the possible contribution from dust heated by a non-stellar ionization source, i.e., the active galactic nucleus (AGN) in the center of the galaxy.

Following the unified model of AGN (where the various types are explained solely by a viewing angle difference; see Antonucci 1993, for details), the hot accretion disk around the galaxies supermassive black hole is surrounded by a dusty, molecular torus. In recent years, there has been considerable effort to characterize the nature of this

obscuring material both theoretically and observationally. Several models have been proposed to explain the observed and inferred properties of the torus, including a smooth, continuous, geometrically and optically thick dusty torus (Krolik & Begelman 1988; Beckert & Duschl 2004; Fritz et al. 2006), full radiative transfer clumpy torus models (e.g., Nenkova et al. 2008a; Schartmann et al. 2008; Mor et al. 2009; Hönig & Kishimoto 2010; Stalevski et al. 2012) and clumpy winds structures originating from the accretion disk (e.g., Elitzur & Shlosman 2006). However, within their uncertainties (e.g., size of the torus, inclination, dust distribution function, etc), almost all these models predict some (non-negligible) torus contribution at the MIR and FIR wavelengths where dust-based SFRs are commonly used under the assumption that the FIR luminosity is attributed solely to star formation (e.g., Fritz et al. 2006; Mullaney et al. 2011). Thus, it is of the utmost importance to determine the AGN contribution to the FIR emission.

To investigate the AGN contribution to the FIR emission, it is important to start with a complete and unbiased sample of local AGN at $z < 0.05$, where we can use *Herschel*'s unique angular resolution to spatially resolve the FIR emission. Given its high energy band selection, 14 to 195 keV, the *Swift*/Burst Alert Telescope (BAT) survey of AGN represents such a sample, because it is unbiased to Compton thin AGN, e.g., sources with Hydrogen column densities of less than a few times 10^{24} cm $^{-2}$. In addition, the BAT AGN survey is not sensitive to stellar activity in the host galaxy, because star formation has a negligible contribution at these hard X-ray energies. Thus, the BAT sample can provide a unique perspective into the AGN and star formation contributions at the FIR wavelengths, where the dusty torus and the current star formation are the competing effects to heat the dust. For this purpose, we performed a statistical study of the correlations between the FIR luminosities observed by the *Herschel* observatory and the hard X-ray luminosities for more than 300 local BAT AGN. In Section 2-3 we present details on the sample selection, *Herschel* Observations and data processing. Section 4 shows the FIR properties of the BAT

sample. Section 5 discusses the observed correlations between the hard X-ray and FIR emission. In Section 6 we present the FIR colors of the BAT sample and their implications for some of the FIR predictions of torus models. Section 7 shows the comparison for the FIR colors between the BAT AGN and normal, star forming galaxies. Finally, Section 8 lists the main conclusions of this work. In order to calculate luminosities we assumed a flat universe with a Hubble constant $H_o = 71 \text{ km s}^{-1} \text{ Mpc}^{-1}$, $\Omega_\Lambda = 0.73$, and $\Omega_M = 0.27$, with redshift values taken from NASA’s ExtraGalactic Database (NED), except for sources with redshift values $z < 0.01$, where distances are taken from The Extragalactic Distance Database (EDD; Tully 1988; Tully et al. 2009).

2. Sample

The sample presented in this work was selected from the low-redshift ($z < 0.05$) 58-month Swift-BAT survey with a median redshift of $z \sim 0.025^2$. The 58-month Swift-BAT is an almost uniform hard X-ray all-sky survey and reaches a flux level of $1.1 \times 10^{-11} \text{ ergs sec}^{-1} \text{ cm}^{-2}$ over 50% of the sky and $1.48 \times 10^{-11} \text{ ergs sec}^{-1} \text{ cm}^{-2}$ over 90% of the sky (Baumgartner et al. 2013). Source identifications are based primarily on the X-ray imaging data and a correlation with optical images and catalogs. In some cases, the identifications are based on positional coincidences with previously known AGN. The main advantage of the BAT AGN sample is that the selection process is completely independent of optical, IR or radio properties of the host galaxy. Our final sample of galaxies includes 149 Seyfert 1 galaxies (1/1.2/1.5), 157 Seyfert 2 galaxies (1.8/1.9/2.0), 6 LINERs and 1 unclassified Seyfert galaxy, ESO 464-G016 (Véron-Cetty & Véron 2010). One must note that some of the Seyfert galaxies have dual classifications, see Table 1. For the purpose of grouping

²<http://swift.gsfc.nasa.gov/results/bs58mon/>

galaxies through the rest of the paper, we take the Seyfert classification as the primary type.

3. Observations and Data Processing

The 58-month BAT sample was observed by the Photodetector Array Camera and Spectrometer (PACS, Poglitsch et al. 2010) on the *Herschel* Space Observatory. The vast majority of the BAT AGN presented in this work are from our cycle 1 open-time program (OT1_rmushot_1, PI: R. Mushotzky) with a total of 291 sources. For the sake of completeness we included 22 BAT sources from different programs publicly available from the Herschel science archive (HSA), see Table 1 for details. From this the total number of BAT AGN sources in our sample is 313. For the sources obtained through our OT1 program the PACS imaging for the blue $70\text{ }\mu\text{m}$ ($60\text{-}85\text{ }\mu\text{m}$) and red $160\text{ }\mu\text{m}$ ($130\text{-}210\text{ }\mu\text{m}$) band was obtained simultaneously in scan mode along two scan map position angles at 70 and 110 degrees. Each orientation angle was scanned with a medium scan speed of $20''\text{ s}^{-1}$, 2 scan legs of $3.0'$ length with $5.0''$ scan leg separation and a repetition factor of 1. The total time per observation was 52 s. From our OT1 program the galaxies II SZ 010, Mrk 290, PG 2304+042 and Mrk 841 have a different configuration with 10 scan legs of $3.0'$ length with $4.0''$ scan leg separation and a repetition factor of 1 with a total time per observation of 276 s.

For the PACS data reduction we use the Herschel Interactive Processing Environment (HIPE, Ott 2010) version 8.0. The “Level 0” observations (raw data) were processed through the standard pipeline procedure to convert from Level 0 to Level 1 data. This procedure includes the extraction of the calibration tree needed for the data processing, correction for electronic crosstalk, application of the flat-field correction and finally deglitching and conversion from Volts to Jy/pixel. In order to correct for bolometer drift

(low frequency noise), both thermal and non-thermal (uncorrelated noise), and to create the final maps from the Level 1 data, we used the algorithm implemented in *Scanamorphos* (v19.0, Roussel 2013), which makes use of the redundancy built in the observations to derive the brightness drifts. Because of this, *Scanamorphos* is independent of any pre-defined noise model because it relies on the fact that each portion of the sky is scanned by multiple bolometers at different times. All final maps have a pixel size of $\sim 1/4$ of the point spread function (PSF) full width at half-maximum (FWHM), i.e., $1.4''$ at $70\text{ }\mu\text{m}$ and $2.85''$ at $160\text{ }\mu\text{m}$. *Scanamorphos* also produces an error and weight map. The error map is defined as the error on the mean brightness in each pixel. It is built using the weighted variance because weights are used for the projection of the final map. The error map does not include any error propagation associated with the different steps performed on the pipeline. On the other hand, the weighted map is built by co-adding the weights and is normalized by the average of the weights. See Figure 10 of the Appendix for a sample of the final maps. All the images are available in electronic form in the on-line version. At the median redshift for the sample, $1''$ represents ~ 500 pc. Hence, for example, PACS $70\mu\text{m}$ PSF will sample about 2.8 kpc at $z \sim 0.025$.

PACS fluxes are measured using a combination of circular and elliptical apertures for sources that are visually identified as point-like (and/or relatively point-like) and extended sources, respectively. The apertures are chosen by eye to contain all of the observed emission at each wavelength. In addition, background subtraction is performed locally with a circular or elliptical annulus around the source. For point-like sources the background annulus was set to be $20''$ to $25''$ and $24''$ to $28''$ in radius for the blue and red camera, respectively. For extended sources, the background annulus was set to encompass a clean, uncontaminated sky region close to the source. Table 1 shows the different aperture sizes used in this work.

Aperture corrections are applied to the background subtracted fluxes. For point-like sources we applied the correction outlined in Table 15 of the technical report PICC-ME-TN-037³. To derive aperture corrections for extended sources we used higher resolution images from *Spitzer*/IRAC 8.0 μm and measured the total flux with the same aperture employed for the PACS analysis. Then we convolved the same image with the right kernel to bring it to the PACS resolution⁴ (Gordon et al. 2008) and remeasured the flux in the same aperture. The ratio of the unconvolved to the convolved (the same PSF as the *Herschel* PACS) flux is used as an estimate of the aperture correction. From the list of extended sources, there are 53 BAT AGN sources with *Spitzer*/IRAC 8.0 μm images available through The Spitzer Enhanced Imaging Products archive. For these sources we find the aperture corrections to be very small, with values not greater than 1.03 (< 3%) and with a mean value very close to unity. Therefore, for large, extended sources without higher resolution images, we apply no correction, so we added a 3% flux uncertainty. Caution must be taken, because aperture corrections derived from this empirical method assume that the spatial distribution is the same at PACS (FIR) and IRAC (MIR) wavelengths.

The total uncertainty for the integrated photometry is a combination of the error on the mean brightness in each pixel added in quadrature within the source aperture (the error map produced by Scanamorphos), the standard deviation of all the pixels in the background aperture and the PACS photometer flux calibration accuracy. In some cases, the dominant source of error is due to background fluctuations especially in sources contaminated by cirrus (see Table 1); however, almost all of our sources have a clean, flat extragalactic field. The PACS calibration uncertainties are σ_{cal} , 5%, according to Version 2.4 of the PACS

³https://nhscdmz2.ipac.caltech.edu/sc/uploads/Pacs/PSF_aperture_corrections_FM6.txt

⁴http://dirty.as.arizona.edu/~kgordon/mips/conv_psfs/conv_psfs.html

Observer’s Manual⁵. Finally, we take as an upper-limit five times the total uncertainty for the integrated photometry (5σ). Table 1 presents the spatially integrated flux densities for all 313 galaxies for PACS blue and red photometric bands. The tabulated flux densities include aperture corrections. No reddening and color corrections have been applied to the data in Table 1. From this, 295 and 260 sources are detected by PACS at 70 and 160 μm , implying a detection rate of 94% and 83%, respectively. Only two sources, namely, MCG-01-09-045 and UGC03995A, are detected at PACS 160 μm with no detections at 70 μm .

To investigate the nature of the 16 undetected sources in both PACS bands, we used values from the *WISE* All-sky source catalog⁶ at 3.4, 4.6, 12, and 22 μm to construct the AGN spectral energy distribution (SED) between 3.4 and 160 μm for the BAT sample. From this, we compared mean and median SEDs for the entire sample with those from the PACS undetected sources. The upper panel in Figure 1 shows a comparison between the SEDs of the sources with detections in both PACS bands and the undetected PACS sources (the individual SED’s of the BAT AGN are normalized to the flux in the *WISE* 22 μm band). It can be seen that the undetected sources are characterized by a flatter infrared SED than that for the entire sample. Note that the entire sample was detected by *WISE*, except for Mrk 3. For the *WISE* fluxes, we selected the magnitude measured with profile-fitting photometry for sources flagged by *WISE* as point-sources, and for extended sources, we selected the magnitude measured via elliptical aperture photometry which are measured using areas that are scaled from the 2MASS Extended Source Catalog morphologies (Skrutskie et al. 2006). In addition, we inspected the low-resolution MIR spectra of 6 PACS undetected sources observed by *Spitzer* (lower panel in Figure1). We

⁵http://herschel.esac.esa.int/Docs/PACS/html/pacs_om.html

⁶<http://irsa.ipac.caltech.edu/Missions/wise.html>

retrieved the low-resolution MIR spectra for these sources, namely, ESO121-IG028, Mrk352, Mrk50, PG2304+042, SBS1301+540 and UM614, via the Cornell atlas of Spitzer/IRS sources (Lebouteiller et al. 2011). From this comparison it is clear that, on average, these sources show a systematic decrease in their MIR emission towards longer wavelengths, $\lambda > 20\mu\text{m}$. Moreover, the low-resolution MIR spectra show no strong star formation features (e.g., polycyclic aromatic hydrocarbon emission). Overall, these results suggest that PACS undetected BAT AGN reside in cold dust depleted systems with no active star formation. We define this group of objects as X-ray Bright Far-infrared Faint sources (XBFF). A more detailed analysis of the BAT SEDs and the nature of the XBFF sources will be presented in subsequent papers in the BAT *Herschel* series.

Figure 2 shows the comparison between the PACS 70 μm measurements and observations from the *Infrared Astronomical Satellite* at 60 μm (*IRAS*, Neugebauer et al. 1984). Note that in most cases, given PACS better photometric sensitivity, it was not possible to find *IRAS* fluxes for all galaxies in the sample. In total, 205 sources from the BAT sample had *IRAS* detections at 60 μm , mainly from the *IRAS* Faint Source Catalog for faint point sources (Moshir et al. 1990), the Point Source Catalog (V2.0, Helou & Walker 1988) and the catalog of large optical galaxies (Rice et al. 1988). From this comparison, we found very good agreement between the PACS and *IRAS* fluxes with S_{60} density fluxes (*IRAS*) slightly below the 1:1 line, as expected (an increasing flux density at wavelengths shorter than the FIR peak, Dale et al. 2001; Dale & Helou 2002; Draine & Li 2007; Casey 2012; Dale et al. 2012). The good correlation between the fluxes suggests that the size of our aperture photometry extractions encompass the FIR emission from the galaxy, because the beam size used for the *IRAS* catalog is larger, approximately 1' at 60 μm , than the majority of the aperture sizes used in this work. This result is corroborated by the spatial analysis presented in Mushotzky et al. (2014), where we show that in the majority of the BAT sources, the bulk of the FIR radiation is point-like at the spatial resolution of

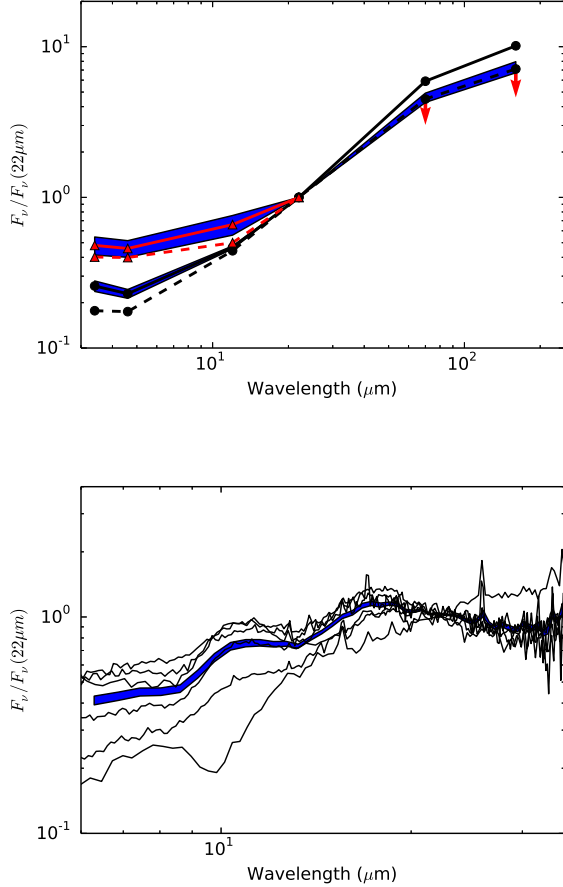


Fig. 1.— Upper panel: comparison of the observed spectral energy distribution, normalized to the flux in the *WISE* 22 μm band, for the entire BAT sample (circles) and that of the PACS undetected sources (triangles, BAT sources undetected in both PACS band, see Table 1). The mean and median of the entire sample are represented by the solid and dashed black lines, respectively. Similarly, the mean and median of the PACS undetected sources are shown as solid and dashed red lines, respectively. The blue shading indicates the standard error of the mean. Lower panel: *Spitzer* low-resolution spectra for a sample of PACS undetected sources observed by *Spitzer*, namely, ESO 121-IG028, Mrk 352, Mrk 50, PG2304+042, SBS1301+540 and UM 614. The individual spectra have been normalized to the flux at 22 μm . The blue shading indicates the standard error of the mean.

Herschel (a median value of 2 kpc FWHM). Note that some of the brightest sources in our sample, e.g., Centaurus A, are extended; thus, the point source extraction from *IRAS*, even at $1'$ resolution, underpredicts the flux at $60\ \mu\text{m}$. On the other hand, there may be contamination from a neighboring source that lies within *IRAS* bigger aperture, thereby, overpredicting the flux at $60\ \mu\text{m}$. For example, there is an IR bright companion source (GALEXASC J154634.12+692844.7) at $\sim 56.4''$ from 2MASXJ15462424+6929102 (see Figure 2).

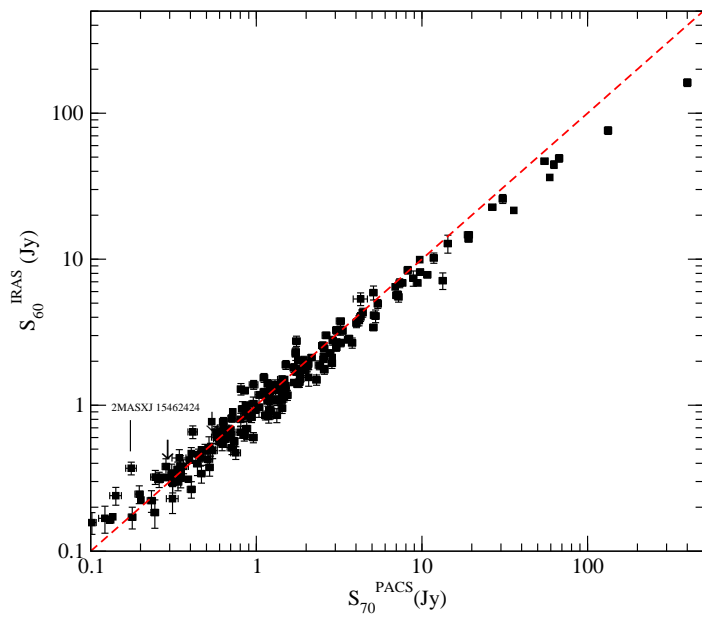


Fig. 2.— Comparison between the PACS fluxes at 70 μm (S_{70}) and the *IRAS* fluxes at 60 μm (S_{60}). It can be seen that the bulk of the *IRAS* flux is contained within the PACS (smaller) apertures. The red dashed line indicates $y = x$.

Table 1. Galaxy Sample and Far-Infrared Flux Densities

Name	RA (J2000.0)	DEC (J2000.0)	Distance Mpc	Type	70μm Jy	160μm Jy	BAT	Aperture 70μm	Aperture 160μm	Program ID
(1)	(2)	(3)	(4)	(5)	(6)	(7)	(8)	(9)	(10)	(11)
Mrk 335	00 06 19.5	+20 12 10	111.10	Sy 1.2	0.309 ± 0.016	0.150 ± 0.010	18.43	12	22	2
2MASX J00253292+6821442	00 25 32.9	+68 21 44	51.15	Sy 2	0.290 ± 0.015	0.303 ± 0.024	18.24	12	22	1
CGCG 535-012	00 36 21.0	+45 39 54	208.70	Sy 1.2	0.145 ± 0.011	< 0.177	15.58	12	22	1
NGC 235A	00 42 52.8	-23 32 28	95.51	Sy 1	2.337 ± 0.123	2.613 ± 0.173	47.65	12	22	1
MCG-02-02-095	00 43 08.8	-11 36 04	80.87	Sy 2	0.081 ± 0.008	< 0.196	8.95	5.5	10.5	1
Mrk 348 ^b	00 48 47.1	+31 57 25	64.24	Sy 2	0.808 ± 0.041	0.995 ± 0.050	156.04	12	22	3
MCG+05-03-013	00 51 35.0	+29 24 05	156.12	Sy 1	0.825 ± 0.046	1.890 ± 0.166	9.81	14	24	1
Mrk 352	00 59 53.3	+31 49 37	63.50	Sy 1	< 0.080	< 0.089	29.98	12	22	1
ESO 195-IG021NED03	01 00 35.0	-47 52 04	211.44	Sy 1.8	0.411 ± 0.021	0.824 ± 0.106	16.30	12	22	1
MCG-07-03-007	01 05 26.8	-42 12 58	129.16	Sy 2	0.313 ± 0.017	0.457 ± 0.029	11.97	12	22	1
2MASX J01064523+0638015	01 06 45.3	+06 38 02	178.71	Sy 2	0.150 ± 0.011	< 0.097	15.45	12	22	1
2MASX J01073963-1139117	01 07 39.6	-11 39 12	207.86	Sy 2	0.491 ± 0.033	0.715 ± 0.060	10.48	12	22	1
NGC 424	01 11 27.6	-38 05 00	50.14	Sy 2	1.687 ± 0.089	1.602 ± 0.144	20.72	12	22	1
Mrk 975	01 13 51.0	+13 16 18	217.74	Sy 1	0.806 ± 0.050	1.279 ± 0.068	16.54	12	22	1
IC 1657	01 14 07.0	-32 39 03	50.95	Sy 2	2.895 ± 0.145	3.950 ± 0.198	14.32	80 33 18	80 33 18	1
Fairall 9 ^b	01 23 45.8	-58 48 21	205.85	Sy 1	0.532 ± 0.039	0.611 ± 0.038	49.46	12	18	1
NGC 526A	01 23 54.4	-35 03 56	81.86	Sy 1.5	0.201 ± 0.013	0.291 ± 0.031	63.25	12	22	1
NGC 513	01 24 26.9	+33 47 58	83.80	Sy 2	2.862 ± 0.146	4.143 ± 0.211	20.35	18	22	1
Mrk 359	01 27 32.6	+19 10 44	74.42	Sy 1.5	1.468 ± 0.078	1.473 ± 0.107	13.32	12	22	1
MCG-03-04-072	01 28 06.7	-18 48 31	201.25	Sy 1	0.115 ± 0.009	0.225 ± 0.017	19.74	12	22	1
ESO 244-IG030	01 29 51.2	-42 19 35	110.27	Sy 2	1.425 ± 0.075	2.207 ± 0.116	8.86	50 22 36	50 22 36	1
ESO 297-018 ^b	01 38 37.2	-40 00 41	108.64	Sy 2	0.681 ± 0.037	1.838 ± 0.094	68.66	145 17 20	145 17 20	1

Table 1—Continued

Name	RA (J2000.0)	DEC (J2000.0)	Distance Mpc	Type	70μm Jy	160μm Jy	BAT	Aperture 70μm	Aperture 160μm	Program ID
(1)	(2)	(3)	(4)	(5)	(6)	(7)	(8)	(9)	(10)	(11)
MCG-01-05-047	01 52 49.0	-03 26 49	73.60	Sy 2	2.403 ± 0.135	6.131 ± 0.312	22.86	340 19 63	340 19 63	1
UGC 01479	02 00 19.1	+24 28 25	70.30	Sy 2	1.748 ± 0.090	2.665 ± 0.135	14.36	0 21 32	0 21 32	1
NGC 788	02 01 06.4	-06 48 56	58.06	Sy 2	0.518 ± 0.027	0.516 ± 0.027	80.13	12	22	1
Mrk 1018	02 06 16.0	-00 17 29	185.16	Sy 1.5	0.068 ± 0.012	0.115 ± 0.015	32.97	5.5	10.5	1
LEDA 138501	02 09 34.3	+52 26 33	215.77	Sy 1	< 0.083	< 0.085	51.28	12	22	1
ESO 197-G027	02 10 52.5	-49 41 55	210.72	Sy 2	0.736 ± 0.038	1.561 ± 0.085	7.88	14	22	1
Mrk 590	02 14 33.6	-00 46 00	113.73	Sy 1.2	0.545 ± 0.036	1.877 ± 0.111	16.66	12	22	1
NGC 931	02 28 14.5	+31 18 42	71.24	Sy 1.5	2.521 ± 0.143	5.331 ± 0.273	60.55	70 30 67	70 30 67	1
IC 1816	02 31 51.0	-36 40 19	72.51	Sy 1.8	1.782 ± 0.099	2.781 ± 0.154	19.25	22	22	1
NGC 985	02 34 37.8	-08 47 15	188.35	Sy 1	1.296 ± 0.070	1.866 ± 0.100	31.90	85 25 30	85 25 30	1
ESO 198-024	02 38 19.7	-52 11 33	198.99	Sy 1	0.106 ± 0.012	< 0.110	29.56	12	22	1
NGC 1052	02 41 04.8	-08 15 21	19.48	Sy 2	0.855 ± 0.048	0.799 ± 0.083	29.46	12	22	1
Mrk 595	02 41 34.9	+07 11 14	116.36	Sy 1.5	0.389 ± 0.020	0.521 ± 0.033	10.86	12	22	1
ESO 479-G031	02 44 47.7	-24 30 50	101.19	L	0.086 ± 0.011	< 0.152	9.05	5.5	10.5	1
HB 890241+622	02 44 57.7	+62 28 07	192.21	Sy 1	0.538 ± 0.027	0.362 ± 0.024	90.54	12	22	1
NGC 1106	02 50 40.5	+41 40 17	61.79	Sy 2	1.112 ± 0.058	1.737 ± 0.123	18.58	12	22	1
2MFGC 02280	02 50 42.6	+54 42 18	64.76	Sy 2	1.541 ± 0.081	2.063 ± 0.137	27.07	12	22	1
NGC 1125 ^b	02 51 40.3	-16 39 04	46.56	Sy 2	3.224 ± 0.164	2.376 ± 0.163	17.43	18	24	1
MCG-02-08-014	02 52 23.4	-08 30 37	71.67	Sy 2	0.337 ± 0.019	0.541 ± 0.041	26.07	12	22	1
ESO 417-G006	02 56 21.5	-32 11 08	69.68	Sy 2	0.244 ± 0.013	0.142 ± 0.027	30.66	12	22	1
MCG-02-08-038	03 00 04.3	-10 49 29	141.14	Sy 1	0.126 ± 0.010	0.340 ± 0.028	17.63	5.5	50 19 30	1
NGC 1194	03 03 49.1	-01 06 13	58.03	Sy 1	0.633 ± 0.034	0.473 ± 0.025	36.58	12	22	1

Table 1—Continued

Name	RA (J2000.0)	DEC (J2000.0)	Distance Mpc	Type	70 μ m Jy	160 μ m Jy	BAT	Aperture 70 μ m	Aperture 160 μ m	Program ID
(1)	(2)	(3)	(4)	(5)	(6)	(7)	(8)	(9)	(10)	(11)
ESO 031-G008	03 07 35.3	-72 50 03	119.17	Sy 1.2	0.069 ± 0.005	< 0.259	12.43	5.5	10.5	1
MCG+00-09-042	03 17 02.2	+01 15 18	102.22	Sy 2 / L	3.793 ± 0.192	4.155 ± 0.241	13.27	12	22	1
IRAS 03219+4031	03 25 13.2	+40 41 55	209.07	Sy 2	1.306 ± 0.069	1.171 ± 0.088	19.41	14	22	1
2MASX J03305218+0538253	03 30 52.2	+05 38 26	201.25	Sy 1	0.222 ± 0.016	0.130 ± 0.020	11.02	5.5	10.5	1
MCG-01-09-045	03 31 23.0	-05 08 30	54.69	Sy 2	< 0.133	0.367 ± 0.025	12.75	12	22	1
NGC 1365	03 33 36.4	-36 08 25	17.93	Sy 1.8	133.097 ± 6.656	217.359 ± 10.871	64.07	30 139 213	30 185 336	3
2MASX J03342453-1513402 ^b	03 34 24.5	-15 13 40	151.59	Sy 1.5	0.610 ± 0.039	0.974 ± 0.079	12.46	12	22	1
ESO 548-G081	03 42 03.7	-21 14 39	61.84	Sy 1	0.960 ± 0.051	2.181 ± 0.132	44.46	18	22	1
LCRS B034324.7-394349 ^b	03 45 12.5	-39 34 29	186.73	Sy 1	0.142 ± 0.011	0.224 ± 0.023	10.36	5.5	10.5	1
2MASX J03502377-5018354 ^b	03 50 23.8	-50 18 36	158.52	Sy 2	0.395 ± 0.027	0.471 ± 0.032	20.89	12	10.5	1
2MASX J03534246+3714077	03 53 42.5	+37 14 07	79.90	Sy 2	0.817 ± 0.046	1.128 ± 0.087	15.33	12	22	1
2MASX J03540948+0249307	03 54 09.5	+02 49 31	156.32	Sy 1	0.183 ± 0.012	< 0.198	12.85	5.5	10.5	1
ESO 549-G049	04 02 25.7	-18 02 51	113.32	Sy 2 / L	3.629 ± 0.188	5.131 ± 0.262	25.16	18	22	1
IRAS 04124-0803	04 14 52.7	-07 55 40	165.97	Sy 1	0.657 ± 0.049	0.439 ± 0.024	21.00	12	22	1
3C 111	04 18 21.3	+38 01 36	212.59	Sy 1	0.266 ± 0.017	0.532 ± 0.062	116.80	12	22	1
ESO 157-G023 ^b	04 22 24.2	-56 13 33	190.09	Sy 2	0.082 ± 0.007	0.588 ± 0.034	21.20	5.5	150 17 28	1
2MASX J04234080+0408017 ^b	04 23 40.8	+04 08 02	196.73	Sy 2	0.574 ± 0.038	0.502 ± 0.028	23.88	12	10.5	1
3C 120	04 33 11.1	+05 21 16	143.01	Sy 1	1.368 ± 0.070	1.639 ± 0.102	94.36	12	22	1
Mrk 618	04 36 22.2	-10 22 34	154.31	Sy 1	3.036 ± 0.166	3.244 ± 0.195	17.75	18	28	1
MCG-02-12-050 ^b	04 38 14.2	-10 47 45	157.89	Sy 1.2	0.603 ± 0.042	1.376 ± 0.076	18.97	40 19 23	40 19 23	1
1RXS J044154.5-082639	04 41 54.1	-08 26 34	192.21	Sy 1	0.176 ± 0.012	0.149 ± 0.024	10.21	12	22	1
UGC 03142	04 43 46.8	+28 58 19	93.00	Sy 1	1.227 ± 0.068	2.659 ± 0.161	45.54	35	35	1

Table 1—Continued

Name	RA (J2000.0)	DEC (J2000.0)	Distance Mpc	Type	70 μ m Jy	160 μ m Jy	BAT BAT	Aperture 70 μ m	Aperture 160 μ m	Program ID
(1)	(2)	(3)	(4)	(5)	(6)	(7)	(8)	(9)	(10)	(11)
2MASX J04440903+2813003	04 44 09.0	+28 13 01	48.00	Sy 2	1.224 ± 0.069	2.411 ± 0.340	52.95	12	22	1
MCG-01-13-025	04 51 41.5	-03 48 33	67.96	Sy 1.2	0.092 ± 0.008	0.160 ± 0.030	31.11	5.5	10.5	1
1RXS J045205.0+493248	04 52 05.0	+49 32 45	125.26	Sy 1	0.354 ± 0.021	0.785 ± 0.086	63.16	12	22	1
CGCG 420-015	04 53 25.8	+04 03 42	126.98	Sy 2	0.648 ± 0.034	0.684 ± 0.061	28.14	12	22	1
ESO 033-G002	04 55 59.0	-75 32 28	77.52	Sy 2	0.697 ± 0.038	0.689 ± 0.083	21.26	12	22	1
2MASX J05020903+0331499	05 02 09.0	+03 31 50	68.37	Sy 1	0.084 ± 0.010	< 0.183	15.31	12	22	1
2MASX J05054575-2351139	05 05 45.7	-23 51 14	152.05	Sy 2 / HII	0.179 ± 0.011	0.142 ± 0.025	60.85	12	22	1
CGCG 468-002NED01 ^b	05 08 19.7	+17 21 48	74.94	Sy 2	2.323 ± 0.119	2.378 ± 0.143	26.03	12	12	1
IRAS 05078+1626	05 10 45.5	+16 29 56	76.56	Sy 1.5	1.175 ± 0.061	0.727 ± 0.090	90.61	12	22	1
ESO 553-G022	05 11 57.8	-18 29 38	183.56	Sy 2	0.082 ± 0.010	0.309 ± 0.036	13.72	12	22	1
ARK 120	05 16 11.4	-00 08 59	141.69	Sy 1	0.685 ± 0.039	1.176 ± 0.097	69.95	12	22	1
MCG-02-14-009	05 16 21.2	-10 33 41	122.84	Sy 1	0.343 ± 0.033	0.813 ± 0.060	13.58	12	22	1
ESO 362-18	05 19 35.8	-32 39 28	53.07	Sy 1.5	1.426 ± 0.073	1.923 ± 0.098	49.31	25	25	1
PICTOR A	05 19 49.7	-45 46 44	152.12	Sy 1 / L	0.130 ± 0.011	0.305 ± 0.023	38.59	12	22	1
2MASX J05240693-1210087 ^b	05 24 06.5	-12 10 00	214.86	Sy 1	0.330 ± 0.021	0.261 ± 0.021	18.34	5.5	10.5	1
ESO 553-G043	05 26 27.3	-21 17 12	119.77	Sy 2	0.122 ± 0.010	< 0.114	13.85	12	22	1
NGC 2110	05 52 11.4	-07 27 22	35.60	Sy 2	5.141 ± 0.261	5.227 ± 0.267	319.13	18	22	1
MCG+08-11-011	05 54 53.6	+46 26 22	87.90	Sy 1.5	2.639 ± 0.142	3.467 ± 0.178	133.44	0 25 54	0 34 58	1
2MASX J05580206-3820043	05 58 02.0	-38 20 05	146.83	Sy 1	0.246 ± 0.016	< 0.199	29.27	5.5	10.5	1
IRAS 05589+2828	06 02 10.7	+28 28 22	142.97	Sy 1	0.959 ± 0.055	0.813 ± 0.094	65.19	12	22	1
ESO 005-G004	06 05 41.6	-86 37 55	22.40	Sy 2	7.616 ± 0.387	22.206 ± 1.111	33.60	95 11 56	95 26 79	1
Mrk 3	06 15 36.3	71 02 15	57.70	Sy 2	3.220 ± 0.183	2.530 ± 0.166	135.71	38	38	7

Table 1—Continued

Name	RA (J2000.0)	DEC (J2000.0)	Distance Mpc	Type	70 μ m Jy	160 μ m Jy	BAT	Aperture 70 μ m	Aperture 160 μ m	Program ID
(1)	(2)	(3)	(4)	(5)	(6)	(7)	(8)	(9)	(10)	(11)
ESO 121-IG028 ^b	06 23 45.6	-60 58 44	176.55	Sy 2	< 0.075	< 0.233	28.12	12	22	1
ESO 426-G002	06 23 46.4	-32 13 00	96.39	Sy 2	0.196 ± 0.011	0.146 ± 0.022	24.36	5.5	10.5	1
6dF J0626586-370559	06 26 58.6	-37 05 59	167.57	Sy 1.5	0.209 ± 0.013	0.442 ± 0.032	11.69	12	22	1
VII Zw 073	06 30 25.6	+63 40 41	180.20	Sy 2	2.056 ± 0.104	1.804 ± 0.138	11.14	12	22	1
UGC 03478	06 32 47.2	+63 40 25	54.46	Sy 1.2	1.465 ± 0.077	3.824 ± 0.197	10.13	50 27 41	50 27 41	1
ESO 490-IG026	06 40 11.7	-25 53 43	106.99	Sy 1.2	1.975 ± 0.102	1.604 ± 0.103	37.42	12	22	1
2MASX J06411806+3249313	06 41 18.0	+32 49 32	205.78	Sy 2	0.087 ± 0.009	< 0.053	35.08	12	22	1
Mrk 6 ^b	06 52 12.3	+74 25 37	80.62	Sy 1.5	1.043 ± 0.061	0.942 ± 0.071	60.60	12	18	1
UGC 03601	06 55 49.5	+40 00 01	73.28	Sy 1.5	0.367 ± 0.020	0.719 ± 0.075	21.38	12	22	1
2MASX J06561197-4919499	06 56 12.0	-49 19 50	178.71	Sy 2	0.259 ± 0.016	0.126 ± 0.023	12.17	5.5	10.5	1
MCG+06-16-028	07 14 03.9	+35 16 45	67.09	Sy 2	2.549 ± 0.128	2.487 ± 0.155	16.71	12	22	1
2MASX J07262635-3554214	07 26 26.4	-35 54 22	127.04	Sy 2	1.113 ± 0.059	< 0.700	23.35	12	22 ^a	1
Mrk 79	07 42 32.8	+49 48 35	95.34	Sy 1.2	1.431 ± 0.088	2.370 ± 0.185	46.57	22	30	1
UGC 03995A ^b	07 44 07.0	+29 14 57	67.60	Sy 2	< 0.093	1.915 ± 0.097	16.98	12	22	1
Mrk 10	07 47 29.1	+60 56 01	126.38	Sy 1.2	0.713 ± 0.040	1.973 ± 0.101	14.80	130 21 31	130 26 37	1
2MASS J07594181-3843560	07 59 41.7	-38 43 57	174.22	Sy 1.2	0.046 ± 0.007	< 0.121	50.64	5.5	10.5	1
2MASX J07595347+2323241	07 59 53.5	+23 23 24	126.06	Sy 2	2.311 ± 0.120	4.943 ± 0.250	34.54	18	22	1
IC 0486	08 00 21.0	+26 36 49	115.89	Sy 1	0.989 ± 0.062	1.483 ± 0.089	32.16	14	22	1
ESO 209-G012	08 01 58.0	-49 46 42	176.44	Sy 1.5	1.039 ± 0.058	2.077 ± 0.107	21.27	28	28	1
2MASX J08032736+0841523	08 03 27.4	+08 41 52	204.87	Sy 1	< 0.079	< 0.112	17.32	12	22	1
Mrk 1210	08 04 05.9	+05 06 50	57.60	Sy 2	1.510 ± 0.078	0.914 ± 0.089	54.44	12	22	1
MCG+02-21-013	08 04 46.4	+10 46 36	149.34	Sy 2	0.713 ± 0.046	1.701 ± 0.103	15.22	12	22	1

| 18 |

Table 1—Continued

Name	RA (J2000.0)	DEC (J2000.0)	Distance Mpc	Type	70 μ m Jy	160 μ m Jy	BAT	Aperture 70 μ m	Aperture 160 μ m	Program ID
(1)	(2)	(3)	(4)	(5)	(6)	(7)	(8)	(9)	(10)	(11)
Fairall 272 ^b	08 23 01.1	-04 56 05	93.70	Sy 2	0.798 ± 0.044	1.222 ± 0.071	46.43	12	22	1
Fairall 1146	08 38 30.8	-35 59 33	136.66	Sy 1.5	1.219 ± 0.068	1.407 ± 0.090	28.91	14	22	1
MCG+11-11-032	08 55 12.5	+64 23 46	157.45	Sy 2	0.113 ± 0.008	0.317 ± 0.020	17.71	12	22	1
NGC 2655	08 55 37.7	+78 13 23	24.40	Sy 2	1.830 ± 0.093	2.862 ± 0.147	13.44	14	24	1
Mrk 18	09 01 58.4	+60 09 06	47.23	Sy 2	2.565 ± 0.133	2.409 ± 0.170	12.21	12	22	1
2MASX J09023729-4813339	09 02 37.3	-48 13 34	170.18	Sy 1	0.092 ± 0.010	< 0.801	29.41	12	22 ^a	1
2MASX J09043699+5536025	09 04 36.9	+55 36 03	161.42	Sy 1	0.181 ± 0.010	< 0.130	15.20	12	22	1
Mrk 704	09 18 26.0	+16 18 19	126.29	Sy 1.5	0.336 ± 0.018	0.253 ± 0.027	33.09	12	22	1
SBS 0915+556 ^b	09 19 13.2	+55 27 55	216.68	Sy 2	0.098 ± 0.013	< 0.075	8.13	5.5	10.5	1
IC 2461	09 19 58.0	+37 11 29	54.18	Sy 1.9	1.446 ± 0.075	3.244 ± 0.164	19.91	48 40 15	48 40 15	1
MCG-01-24-012 ^b	09 20 46.2	-08 03 22	84.24	Sy 2	0.572 ± 0.031	1.091 ± 0.136	40.82	5.5	34	1
MCG+04-22-042	09 23 43.0	+22 54 33	140.08	Sy 1.2	0.131 ± 0.012	0.399 ± 0.027	39.86	5.5	0 16 28	1
2MASX J09235371-3141305	09 23 53.7	-31 41 31	184.85	Sy 1.9	0.110 ± 0.007	< 0.163	19.16	12	22	1
2MASX J09254750+6927532	09 25 47.5	+69 27 53	169.73	Sy 1	0.086 ± 0.009	< 0.200	9.23	5.5	10.5	1
NGC 2885	09 27 18.5	+23 01 12	113.43	Sy 1	0.233 ± 0.013	0.648 ± 0.057	15.91	12	22	1
CGCG 312-012	09 29 37.9	+62 32 39	110.33	Sy 2	0.071 ± 0.006	0.189 ± 0.027	9.04	12	22	1
ESO 565-G019 ^b	09 34 43.6	-21 55 40	69.65	Sy 2	3.045 ± 0.155	3.029 ± 0.154	20.68	18	18	1
2MASX J09360622-6548336 ^b	09 36 06.3	-65 48 33	170.72	Sy 1.8	< 0.074	< 0.118	12.97	12	22	1
CGCG 122-055	09 42 04.8	+23 41 07	91.76	Sy 1	0.651 ± 0.040	0.572 ± 0.039	13.76	12	22	1
NGC 2992 ^b	09 45 42.1	-14 19 35	31.60	Sy 2	9.456 ± 0.480	12.119 ± 0.755	26.89	35	60	3
MCG-05-23-016	09 47 40.2	-30 56 55	36.10	Sy 2	1.454 ± 0.074	0.477 ± 0.031	201.30	12	22	1
NGC 3035	09 51 55.0	-06 49 23	62.03	Sy 1.8	0.803 ± 0.049	2.633 ± 0.134	19.32	144 31 42	144 31 42	1

Table 1—Continued

Name	RA (J2000.0)	DEC (J2000.0)	Distance Mpc	Type	70μm Jy	160μm Jy	BAT	Aperture 70μm	Aperture 160μm	Program
(1)	(2)	(3)	(4)	(5)	(6)	(7)	(8)	(9)	(10)	(11)
NGC 3081	09 59 29.5	-22 49 35	32.50	Sy 2	2.657 ± 0.134	3.992 ± 0.202	83.17	80 35 49	80 35 49	3
2MASX J09594263-3112581	09 59 42.6	-31 12 58	160.78	Sy 1	0.282 ± 0.018	0.270 ± 0.027	17.24	12	22	1
NGC 3079	10 01 57.8	+55 40 47	19.13	Sy 2	62.729 ± 2.155	98.058 ± 4.778	33.03	170 34 113	170 34 113	1
ESO 499-G041	10 05 55.4	-23 03 25	54.67	Sy 1.5	0.540 ± 0.028	0.940 ± 0.137	14.63	12	22	1
ESO 263-G013	10 09 48.2	-42 48 40	145.35	Sy 2	0.165 ± 0.011	< 0.196	35.35	5.5	10.5	1
ESO 374-G044	10 13 19.9	-35 58 58	122.84	Sy 2	0.285 ± 0.015	0.326 ± 0.032	20.07	12	22	1
ARK 241	10 21 40.2	-03 27 14	178.01	Sy 1	0.081 ± 0.005	< 0.178	20.41	12	22	1
NGC 3227	10 23 30.6	+19 51 54	20.85	Sy 1.5	10.781 ± 0.544	21.675 ± 1.091	109.94	152 64 87	152 64 87	5
NGC 3281	10 31 52.1	-34 51 13	45.45	Sy 2	7.342 ± 0.369	7.006 ± 0.361	86.41	24	45	3
2MASX J10402231-4625264	10 40 22.5	-46 25 26	102.93	Sy 2	1.202 ± 0.064	1.407 ± 0.105	24.93	12	22	1
SDSS J104326.47+110524.2	10 43 26.5	+11 05 24	208.41	Sy 1	0.058 ± 0.010	< 0.140	14.17	12	22	1
MCG+12-10-067	10 44 08.5	+70 24 19	145.53	Sy 2	0.869 ± 0.046	1.908 ± 0.099	12.88	15 19 32	15 19 32	1
MCG+06-24-008	10 44 49.0	+38 10 52	111.52	Sy 1.9	0.752 ± 0.051	1.850 ± 0.104	13.98	14	22	1
UGC 05881	10 46 42.5	+25 55 54	88.36	Sy 2	1.891 ± 0.096	2.002 ± 0.128	19.31	12	22	1
NGC 3393	10 48 23.5	-25 09 43	53.34	Sy 2	1.731 ± 0.088	3.780 ± 0.196	25.98	18	55	1
Mrk 417	10 49 30.9	+22 57 52	141.88	Sy 2	0.132 ± 0.008	0.118 ± 0.020	32.40	5.5	10.5	1
NGC 3431	10 51 15.0	-17 00 29	75.01	Sy 2	0.665 ± 0.051	1.745 ± 0.098	22.43	130 17 39	130 17 39	1
Mrk 728	11 01 01.8	+11 02 49	154.74	Sy 1.9	0.046 ± 0.005	< 0.062	13.72	5.5	10.5	1
NGC 3516	11 06 47.5	+72 34 07	38.90	Sy 1.5	1.804 ± 0.092	1.196 ± 0.090	118.34	12	22	1
IC 2637	11 13 49.7	+09 35 11	126.27	Sy 1.5	2.576 ± 0.136	4.187 ± 0.221	12.39	18	22	1
ARP 151	11 25 36.2	+54 22 57	90.54	Sy 1	< 0.048	< 0.070	19.57	5.5	10.5	1
ESO 439-G009 ^b	11 27 23.4	-29 15 27	102.78	Sy 2	0.600 ± 0.044	1.486 ± 0.078	6.71	102 19 24	102 19 24	1

Table 1—Continued

Name	RA (J2000.0)	DEC (J2000.0)	Distance Mpc	Type	70μm Jy	160μm Jy	BAT	Aperture 70μm	Aperture 160μm	Program ID
(1)	(2)	(3)	(4)	(5)	(6)	(7)	(8)	(9)	(10)	(11)
NGC 3718	11 32 34.9	+53 04 05	17.00	L	0.632 ± 0.051	3.709 ± 0.240	12.09	14	130 23 100	1
IC 2921	11 32 49.3	+10 17 47	192.38	Sy 1	0.090 ± 0.011	< 0.172	15.64	5.5	10.5	1
Mrk 739E	11 36 29.4	+21 35 46	128.42	Sy 1	1.683 ± 0.085	3.130 ± 0.179	13.19	14	22	1
IGR J11366-6002	11 36 42.0	-60 03 07	59.77	Sy 2 / L	1.142 ± 0.059	1.587 ± 0.090	20.69	12	22	1
NGC 3783	11 39 01.8	-37 44 19	38.50	Sy 1	3.046 ± 0.157	4.491 ± 0.270	181.11	40	40	3
NGC 3786 ^b	11 39 42.6	+31 54 33	46.18	Sy 1.8	2.190 ± 0.205	3.138 ± 0.454	18.02	60 19 29	60 19 29	1
KUG 1141+371	11 44 29.9	+36 53 09	165.52	Sy 1	0.045 ± 0.009	< 0.098	15.38	5.5	10.5	1
UGC 06728	11 45 16.0	+79 40 53	27.70	Sy 1.2	0.104 ± 0.008	< 0.087	27.20	12	22	1
2MASX J11454045-1827149	11 45 40.5	-18 27 16	142.74	Sy 1	0.312 ± 0.026	0.339 ± 0.024	53.26	12	22	1
MCG+05-28-032 ^b	11 48 45.9	+29 38 28	98.95	L	0.876 ± 0.049	1.381 ± 0.121	24.48	12	22	1
MCG-01-30-041	11 52 38.2	-05 12 26	80.63	Sy 1.8	1.497 ± 0.077	1.751 ± 0.124	14.02	12	22	1
2MASX J12005792+0648226	12 00 57.9	+06 48 23	156.52	Sy 2	0.522 ± 0.027	0.917 ± 0.060	21.18	12	22	1
Mrk 1310	12 01 14.4	-03 40 41	83.87	Sy 1	0.137 ± 0.011	0.268 ± 0.026	11.32	12	22	1
LEDA 38038	12 02 47.6	-53 50 08	120.69	Sy 2	1.951 ± 0.102	1.413 ± 0.126	48.02	12	22	1
NGC 4051	12 03 09.6	+44 31 53	14.58	Sy 1.5	13.365 ± 0.675	38.655 ± 1.943	39.54	120 104 133	120 104 133	5
ARK 347	12 04 29.7	+20 18 58	96.46	Sy 2	0.365 ± 0.019	0.497 ± 0.030	29.48	12	22	1
UGC 07064 ^b	12 04 43.3	+31 10 38	107.64	Sy 1.9	1.749 ± 0.092	3.089 ± 0.175	13.27	14	22	1
NGC 4102	12 06 23.0	+52 42 40	20.38	L	55.005 ± 2.751	54.194 ± 2.710	27.90	35 45 55	35 45 55	1
Mrk 198	12 09 14.1	+47 03 30	104.23	Sy 2	0.846 ± 0.050	1.025 ± 0.065	22.22	12	22	1
NGC 4138	12 09 29.8	+43 41 07	15.57	Sy 1.9	2.063 ± 0.129	5.537 ± 0.459	30.00	147 32 45	147 32 45	1
NGC 4151 ^b	12 10 32.6	+39 24 21	9.90	Sy 1.5	6.889 ± 0.354	9.055 ± 0.460	538.93	135 64 96	135 64 96	4
KUG 1208+386	12 10 44.3	+38 20 10	97.97	Sy 1	0.195 ± 0.014	< 0.163	20.69	5.5	10.5	1

Table 1—Continued

Name	RA (J2000.0)	DEC (J2000.0)	Distance Mpc	Type	70 μ m Jy	160 μ m Jy	BAT	Aperture 70 μ m	Aperture 160 μ m	Program ID
(1)	(2)	(3)	(4)	(5)	(6)	(7)	(8)	(9)	(10)	(11)
NGC 4180	12 13 03.0	+07 02 20	40.08	Sy 2	5.250 ± 0.264	8.980 ± 0.451	16.66	40 29 39	40 29 39	1
NGC 4235	12 17 09.9	+07 11 30	24.97	Sy 1	0.349 ± 0.018	0.823 ± 0.130	32.45	12	22	1
Mrk 202	12 17 55.0	+58 39 35	90.21	Sy 1	0.197 ± 0.012	0.295 ± 0.024	8.07	12	22	1
Mrk 766	12 18 26.5	+29 48 46	55.15	Sy 1.5	4.259 ± 0.216	2.941 ± 0.192	21.67	12	22	1
MESSIER 106	12 18 57.5	+47 18 14	7.44	Sy 1.9 / L	35.872 ± 0.761	105.177 ± 2.314	22.00	160 158 376	160 158 376	3
Mrk 50	12 23 24.1	+02 40 45	100.78	Sy 1	< 0.055	< 0.142	22.62	12	22	1
NGC 4388	12 25 46.7	+12 39 44	21.37	Sy 2	11.796 ± 0.594	18.588 ± 0.933	277.38	92 44 78	92 44 78	5
2MASX J12313717-4758019	12 31 37.2	-47 58 02	119.31	Sy 1	1.507 ± 0.079	1.955 ± 0.119	15.52	12	22	1
2MASX J12335145-2103448	12 33 51.4	-21 03 45	99.04	Sy 1	0.349 ± 0.018	0.286 ± 0.028	9.89	12	22	1
NGC 4507	12 35 36.6	-39 54 33	50.30	Sy 2	4.392 ± 0.221	4.677 ± 0.241	188.11	35	35	1
ESO 506-G027	12 38 54.6	-27 18 28	107.75	Sy 2	0.529 ± 0.036	1.219 ± 0.066	93.94	12	76 17 37	1
LEDA 170194 ^b	12 39 06.3	-16 10 47	159.33	Sy 2	0.373 ± 0.022	0.638 ± 0.046	41.15	12	22	1
Mrk 653	12 39 51.7	+34 58 30	188.01	Sy 2	0.136 ± 0.009	0.412 ± 0.025	9.00	12	22	1
WKK 1263	12 41 25.7	-57 50 04	105.15	Sy 1.5	0.728 ± 0.040	1.005 ± 0.089	46.66	12	22	1
NGC 4619	12 41 44.5	+35 03 46	99.35	Sy 1	1.339 ± 0.072	3.236 ± 0.165	7.02	0 27 33	0 27 33	1
2MASX J12475784-5829599 ^b	12 47 57.8	-58 30 00	120.84	Sy 1.9	< 0.093	< 0.081	9.56	12	22	1
NGC 4748	12 52 12.5	-13 24 53	62.49	Sy 1	1.437 ± 0.073	2.416 ± 0.137	13.78	12	22	1
MCG-01-33-063	13 00 19.1	-08 05 15	113.32	Sy 2	0.302 ± 0.027	1.160 ± 0.062	10.32	350 9 23	350 15 33	1
SBS 1301+540	13 03 59.5	+53 47 30	129.23	Sy 1	< 0.151	< 0.085	32.61	12	22	1
NGC 4941	13 04 13.1	-05 33 06	18.22	Sy 2	0.965 ± 0.058	3.955 ± 0.216	20.45	12	16 41 71	1
NGC 4939	13 04 14.4	-10 20 23	44.16	Sy 2	1.938 ± 0.123	7.000 ± 0.379	24.85	0 49 72	0 49 72	1
ESO 323-077	13 06 26.1	-40 24 53	64.15	Sy 1.2	7.017 ± 0.354	7.531 ± 0.455	33.06	12	22	1

| 22

Table 1—Continued

Name	RA (J2000.0)	DEC (J2000.0)	Distance Mpc	Type	70μm Jy	160μm Jy	BAT	Aperture 70μm	Aperture 160μm	Program ID
(1)	(2)	(3)	(4)	(5)	(6)	(7)	(8)	(9)	(10)	(11)
NGC 4992	13 09 05.6	+11 38 03	108.25	Sy 2	0.180 ± 0.010	0.548 ± 0.047	53.47	5.5	0 21 30	1
II SZ 010	13 13 05.8	-11 07 42	148.60	Sy 1	0.085 ± 0.006	0.125 ± 0.013	15.20	12	22	1
NGC 5033	13 13 27.5	+36 35 38	19.64	Sy 1.9	19.133 ± 0.959	50.152 ± 2.534	5.52	170 31 68	170 54 83	1
UGC 08327NED02 ^b	13 15 17.3	+44 24 26	158.79	Sy 2	1.483 ± 0.077	0.884 ± 0.092	17.08	12	18	1
NGC 5106 ^b	13 20 59.6	+08 58 42	138.27	L	2.872 ± 0.153	5.005 ± 0.258	13.97	18	22	1
MCG-03-34-064	13 22 24.5	-16 43 42	70.76	Sy 1.8	5.099 ± 0.257	3.444 ± 0.198	30.53	12	22	1
Centaurus A	13 25 27.6	-43 01 09	3.66	Sy 2	400.576 ± 20.031	732.884 ± 36.647	1388.99	123 100 261	100 146 367	4
ESO 509-G038	13 31 13.9	-25 24 10	111.91	Sy 1	0.441 ± 0.023	0.732 ± 0.079	14.24	12	22	1
ESO 383-18	13 33 26.1	-34 00 53	52.93	Sy 2	0.654 ± 0.041	0.753 ± 0.070	18.87	12	22	1
ESO 509-IG066NED01 ^b	13 34 39.6	-23 26 48	148.78	Sy 2	0.883 ± 0.048	1.656 ± 0.154	18.18	10	26	1
NGC 5231	13 35 48.2	+02 59 56	93.46	Sy 2	0.702 ± 0.039	1.771 ± 0.125	15.62	12	22	1
MCG-06-30-015	13 35 53.7	-34 17 44	32.90	Sy 1.2	1.205 ± 0.063	0.762 ± 0.068	63.33	12	22	1
NGC 5252	13 38 16.0	+04 32 33	98.77	Sy 1.9	0.341 ± 0.023	0.298 ± 0.030	115.48	12	22	1
2MASX J13411287-1438407	13 41 12.9	-14 38 41	182.26	Sy 1	0.132 ± 0.009	0.198 ± 0.022	24.07	12	16	1
NGC 5273	13 42 08.3	+35 39 15	15.96	Sy 1.9	0.721 ± 0.040	0.705 ± 0.063	13.91	12	22	1
CGCG 102-048	13 44 15.7	+19 34 00	116.73	Sy 1.9	0.052 ± 0.008	< 0.147	19.51	5.5	10.5	1
NGC 5290	13 45 19.2	+41 42 45	34.98	Sy 2	2.071 ± 0.240	7.339 ± 1.290	19.17	272 19 76	272 19 76	1
4U 1344-60	13 47 36.0	-60 37 04	54.94	Sy 1.5	2.040 ± 0.116	< 1.923	107.52	12	22 ^a	1
IC 4329A	13 49 19.3	-30 18 34	68.65	Sy 1.2	1.797 ± 0.095	0.968 ± 0.121	290.49	12	22	1
UM 614	13 49 52.8	+02 04 45	141.64	Sy 1	< 0.061	< 0.103	16.18	12	22	1
2MASX J13512953-1813468	13 51 29.5	-18 13 47	52.09	Sy 1	< 0.076	< 0.079	17.88	12	22	1
Mrk 279 ^b	13 53 03.4	+69 18 30	131.67	Sy 1.5	0.852 ± 0.044	0.822 ± 0.073	39.20	12	22	1

| 23 |

Table 1—Continued

Name	RA (J2000.0)	DEC (J2000.0)	Distance Mpc	Type	70 μ m Jy	160 μ m Jy	BAT	Aperture 70 μ m	Aperture 160 μ m	Program ID
(1)	(2)	(3)	(4)	(5)	(6)	(7)	(8)	(9)	(10)	(11)
ESO 578-G009	13 56 36.7	-19 31 45	151.96	Sy 1	0.318 ± 0.030	0.999 ± 0.075	16.90	18	22	1
2MASX J14080674-3023537	14 08 06.8	-30 23 54	100.88	Sy 1.5	< 0.043	< 0.134	17.19	12	22	1
NGC 5506	14 13 14.9	-03 12 27	23.83	Sy 1.9	8.214 ± 0.414	6.768 ± 0.352	241.03	93 26 57	93 26 57	3
NGC 5548	14 17 59.5	+25 08 12	73.51	Sy 1.5	1.173 ± 0.064	1.494 ± 0.098	78.64	12	22	1
ESO 511-G030	14 19 22.4	-26 38 41	96.21	Sy 1	0.405 ± 0.010	2.021 ± 0.132	39.88	160 34 54	160 34 54	1
NGC 5610	14 24 22.9	+24 36 51	72.26	Sy 2	5.419 ± 0.275	6.219 ± 0.315	19.21	270 23 34	270 23 34	1
NGC 5674	14 33 52.2	+05 27 30	107.35	Sy 1.9	1.819 ± 0.098	3.940 ± 0.202	15.97	0 34 39	0 34 39	1
NGC 5683	14 34 52.4	+48 39 43	157.31	Sy 1	0.097 ± 0.010	< 0.169	12.27	5.5	10.5	1
Mrk 817	14 36 22.1	+58 47 39	136.11	Sy 1.5	2.159 ± 0.110	1.706 ± 0.154	25.91	12	22	1
Mrk 477 ^b	14 40 38.1	+53 30 16	164.03	Sy 1	1.307 ± 0.070	0.735 ± 0.047	14.40	12	10.5	1
NGC 5728	14 42 23.9	-17 15 11	30.57	Sy 2	9.758 ± 0.489	13.717 ± 0.687	88.63	30 38 75	30 38 75	3
WKK 4374	14 51 33.1	-55 40 38	77.09	Sy 2	0.277 ± 0.019	< 0.763	40.84	12	22 ^a	1
2MASX J14530794+2554327	14 53 07.9	+25 54 33	203.52	Sy 1	< 0.131	< 0.129	24.01	12	22	1
WKK 4438	14 55 17.4	-51 34 15	68.42	Sy 1	0.858 ± 0.056	1.592 ± 0.158	21.51	14	22	1
IC 4518A ^b	14 57 41.2	-43 07 56	69.55	Sy 2	5.209 ± 0.261	5.011 ± 0.251	27.75	14	14	1
Mrk 841	15 04 01.2	+10 26 16	158.20	Sy 1	0.448 ± 0.023	0.182 ± 0.014	35.57	12	22	1
Mrk 1392	15 05 56.6	+03 42 26	156.92	Sy 1	0.364 ± 0.026	0.936 ± 0.063	19.01	12	22	1
2MASX J15064412+0351444	15 06 44.1	+03 51 44	163.91	Sy 2	0.064 ± 0.006	< 0.148	15.67	5.5	10.5	1
2MASX J15115979-2119015	15 11 59.8	-21 19 02	194.95	Sy 1	1.846 ± 0.094	1.572 ± 0.122	31.30	12	22	1
NGC 5899	15 15 03.2	+42 02 59	38.08	Sy 2	5.097 ± 0.262	13.193 ± 0.665	20.08	21 31 69	21 31 69	1
CGCG 319-007 ^b	15 19 33.7	+65 35 59	192.21	Sy 1.9	0.345 ± 0.022	0.760 ± 0.068	13.23	12	22	1
MCG-01-40-001	15 33 20.7	-08 42 02	97.60	Sy 2	2.056 ± 0.108	2.425 ± 0.125	32.72	78 21 40	78 21 40	1

Table 1—Continued

Name	RA (J2000.0)	DEC (J2000.0)	Distance Mpc	Type	70μm Jy	160μm Jy	BAT	Aperture 70μm	Aperture 160μm	Program ID
(1)	(2)	(3)	(4)	(5)	(6)	(7)	(8)	(9)	(10)	(11)
Mrk 290	15 35 52.4	+57 54 09	127.80	Sy 1	0.178 ± 0.010	0.116 ± 0.008	23.31	12	22	1
2MASX J15462424+6929102 ^b	15 46 24.3	+69 29 10	162.52	Sy 1.9	0.176 ± 0.013	0.097 ± 0.019	13.94	5.5	10.5	1
NGC 5995	15 48 25.0	-13 45 28	108.50	Sy 2	4.025 ± 0.202	5.399 ± 0.273	43.66	30	30	1
WKK 6092	16 11 51.4	-60 37 55	66.85	Sy 1	0.196 ± 0.014	< 0.058	32.15	12	22	1
WKK 6471	16 18 36.4	-59 27 17	150.20	Sy 1	0.084 ± 0.008	0.519 ± 0.054	21.36	12	22	1
CGCG 367-009	16 19 19.3	+81 02 48	102.90	Sy 2	0.059 ± 0.007	0.154 ± 0.029	22.71	5.5	10.5	1
Mrk 885	16 29 48.3	+67 22 42	109.09	Sy 1	0.406 ± 0.023	1.002 ± 0.085	13.96	12	22	1
ESO 137-34	16 35 14.1	-58 04 48	32.95	Sy 2	2.793 ± 0.150	6.220 ± 0.386	28.19	53	53	1
2MASX J16481523-3035037	16 48 15.3	-30 35 04	134.10	Sy 1	0.096 ± 0.008	< 0.136	45.69	12	22	1
LEDA 214543	16 50 42.7	+04 36 18	138.79	Sy 2	0.118 ± 0.008	0.326 ± 0.022	24.49	12	22	1
UGC 10593	16 52 18.9	+55 54 20	125.92	Sy 2	0.510 ± 0.035	0.917 ± 0.064	15.15	12	22	1
NGC 6221	16 52 46.1	-59 13 07	12.34	Sy 2	59.107 ± 2.976	83.425 ± 6.715	20.16	175 72 103	175 72 103	1
NGC 6240	16 52 58.9	+02 24 03	105.37	Sy 2	26.621 ± 1.358	20.233 ± 1.028	72.21	24	24	6
NGC 6300	17 16 59.5	-62 49 14	15.06	Sy 2	19.113 ± 1.091	44.229 ± 2.621	99.43	120 73 90	120 73 90	1
ARP 102B	17 19 14.5	+48 58 49	103.99	Sy 1 / L	0.103 ± 0.009	< 0.133	18.20	5.5	10.5	1
AX J1737.4-2907	17 37 28.4	-29 08 03	91.89	Sy 1	0.451 ± 0.029	< 0.617	115.86	12	22 ^a	1
ESO 139-G012	17 37 39.1	-59 56 27	72.83	Sy 2	0.414 ± 0.027	2.704 ± 0.142	22.55	12	30 41 58	1
2E1739.1-1210	17 41 55.3	-12 11 57	160.78	Sy 1	0.561 ± 0.028	0.781 ± 0.114	44.50	12	22	1
CGCG 300-062	17 43 17.4	+62 50 21	142.96	Sy 2	0.102 ± 0.006	0.286 ± 0.021	10.08	12	22	1
2MASS J17485512-3254521	17 48 55.1	-32 54 52	85.79	Sy 1	< 0.140	< 0.240	36.66	12	22	1
NGC 6552	18 00 07.3	+66 36 54	114.20	Sy 2	2.574 ± 0.132	2.188 ± 0.143	19.19	12	22	1
2MASXI J1802473-145454	18 02 47.3	-14 54 55	14.40	Sy 1	1.203 ± 0.063	1.872 ± 0.229	40.33	12	22	1

| 25 |

Table 1—Continued

Name	RA (J2000.0)	DEC (J2000.0)	Distance Mpc	Type	70 μ m Jy	160 μ m Jy	BAT BAT	Aperture 70 μ m	Aperture 160 μ m	Program ID
(1)	(2)	(3)	(4)	(5)	(6)	(7)	(8)	(9)	(10)	(11)
UGC 11185NED02 ^b	18 16 11.5	+42 39 37	179.63	Sy 2	0.467 ± 0.031	0.465 ± 0.027	19.22	12	10.5	1
IC 4709	18 24 19.4	-56 22 09	72.34	Sy 2	0.592 ± 0.040	0.943 ± 0.051	42.55	0 13 28	0 20 50	1
Fairall 49	18 36 58.3	-59 24 09	85.88	Sy 2	3.318 ± 0.169	2.555 ± 0.147	14.16	12	22	1
ESO 103-035	18 38 20.3	-65 25 39	56.69	Sy 2	1.732 ± 0.088	0.551 ± 0.034	111.73	12	22	1
Fairall 51	18 44 54.0	-62 21 53	60.54	Sy 1	2.032 ± 0.104	1.753 ± 0.104	40.36	12	22	1
CGCG 341-006	18 45 26.2	+72 11 02	202.61	Sy 2	1.135 ± 0.060	0.957 ± 0.098	11.54	12	22	1
2MASX J18570768-7828212	18 57 07.8	-78 28 21	183.20	Sy 1	0.349 ± 0.019	0.356 ± 0.031	24.22	12	22	1
CGCG 229-015	19 05 25.9	+42 27 40	120.31	Sy 1	0.148 ± 0.009	0.270 ± 0.022	11.14	12	22	1
ESO 141-G055	19 21 14.1	-58 40 13	161.27	Sy 1	0.613 ± 0.041	1.310 ± 0.088	54.42	12	22	1
2MASX J19373299-0613046	19 37 33.0	-06 13 05	43.65	Sy 1.5	3.588 ± 0.184	4.964 ± 0.272	23.21	18	22	1
2MASX J19380437-5109497	19 38 04.4	-51 09 50	174.30	Sy 1.2	0.078 ± 0.010	0.211 ± 0.024	15.05	5.5	10.5	1
NGC 6814	19 42 40.6	-10 19 25	22.80	Sy 1.5	7.224 ± 0.370	16.265 ± 0.824	77.27	96 55 58	96 55 58	1
2MASX J20005575-1810274	20 00 55.7	-18 10 27	161.32	Sy 1	0.886 ± 0.046	0.696 ± 0.062	20.90	12	22	1
ESO 399-20	20 06 57.7	-34 32 58	107.43	Sy 1	0.622 ± 0.040	1.441 ± 0.074	17.93	26	26	1
NGC 6860	20 08 46.9	-61 06 01	63.59	Sy 1	1.431 ± 0.076	3.059 ± 0.160	53.18	22	26	3
2MASX J20101740+4800214	20 10 17.4	+48 00 21	110.41	Sy 2	0.198 ± 0.012	0.352 ± 0.033	13.26	12	22	1
2MASX J20183871+4041003	20 18 38.7	+40 41 00	61.50	Sy 2	< 0.371	< 0.611	28.47	12 ^a	22 ^a	1
II Zw 083	20 26 55.9	-02 16 39	125.89	Sy 2	1.162 ± 0.061	1.306 ± 0.098	12.59	12	22	1
MCG+04-48-002 ^b	20 28 35.1	+25 44 00	59.34	Sy 2	9.698 ± 0.486	10.445 ± 0.524	77.79	60 22 33	60 22 33	1
Mrk 509	20 44 09.7	-10 43 25	149.18	Sy 1.2	1.501 ± 0.078	1.230 ± 0.088	96.16	12	22	1
IC 5063	20 52 02.3	-57 04 08	48.35	Sy 2	4.266 ± 0.419	3.603 ± 0.280	72.57	120 27 44	120 39 69	3
ESO 464-G016	21 02 23.8	-28 10 29	157.89	AGN	0.466 ± 0.024	0.524 ± 0.028	14.10	12	22	1

Table 1—Continued

Name	RA (J2000.0)	DEC (J2000.0)	Distance Mpc	Type	70 μ m Jy	160 μ m Jy	BAT	Aperture 70 μ m	Aperture 160 μ m	Program ID
(1)	(2)	(3)	(4)	(5)	(6)	(7)	(8)	(9)	(10)	(11)
2MASX J21090996-0940147	21 09 10.0	-09 40 15	114.30	Sy 1.2 / L	0.307 ± 0.018	0.229 ± 0.030	19.75	12	22	1
SWIFT J212745.6+565636	21 27 44.9	+56 56 40	62.79	Sy 1	0.156 ± 0.010	< 0.050	37.27	12	22	1
6dF J2132022-334254 ^b	21 32 02.2	-33 42 54	129.56	Sy 1	0.079 ± 0.007	< 0.082	42.69	5.5	10.5	1
2MASX J21355399+4728217	21 35 54.0	+47 28 22	107.65	Sy 1	0.518 ± 0.037	0.749 ± 0.100	22.24	12	22	1
CGCG 493-002	21 38 33.4	+32 05 06	106.77	Sy 1.5	0.426 ± 0.045	0.419 ± 0.025	17.92	12	22	1
NGC 7172	22 02 01.9	-31 52 11	33.90	Sy 2	7.148 ± 0.362	12.693 ± 0.641	170.93	98 29 63	98 29 63	5
NGC 7213	22 09 16.3	-47 10 00	22.00	Sy 1.5	3.237 ± 0.165	7.961 ± 0.401	42.10	50	50	1
MCG+02-57-002	22 23 45.0	+11 50 09	125.26	Sy 1.5	0.539 ± 0.027	0.667 ± 0.081	14.18	12	22	1
MCG+06-49-019	22 27 05.8	+36 21 42	91.58	Sy 2	0.142 ± 0.013	0.517 ± 0.039	19.77	5.5	80 17 28	1
ESO 533-G050	22 34 49.8	-25 40 37	114.00	Sy 2	0.103 ± 0.015	0.398 ± 0.029	13.55	5.5	20 18 29	1
MCG+01-57-016	22 40 17.0	+08 03 14	107.53	Sy 1.8	0.936 ± 0.051	0.966 ± 0.108	16.64	12	22	1
UGC 12237	22 54 19.7	+11 46 57	122.05	Sy 2	0.640 ± 0.040	1.083 ± 0.068	17.11	90 19 52	90 19 52	1
UGC 12282	22 58 55.5	+40 55 53	72.71	Sy 1.9	1.189 ± 0.071	3.685 ± 0.189	19.20	186 18 49	186 18 49	1
KAZ 320	22 59 32.9	+24 55 06	149.64	Sy 1	0.366 ± 0.020	0.308 ± 0.029	24.97	12	22	1
NGC 7465	23 02 01.0	+15 57 53	27.20	L	4.169 ± 0.211	4.715 ± 0.241	14.56	12	22	1
NGC 7469 ^b	23 03 15.6	+08 52 26	69.79	Sy 1.2	30.770 ± 1.540	26.935 ± 1.499	66.74	18	40	3
Mrk 926	23 04 43.5	-08 41 09	205.15	Sy 1.5	0.606 ± 0.033	0.713 ± 0.067	113.89	12	22	1
NGC 7479	23 04 56.7	+12 19 22	33.85	Sy 2 / L	14.341 ± 0.723	25.989 ± 1.307	20.36	40 53 86	40 82 88	1
PG 2304+042 ^b	23 07 02.9	+04 32 57	183.20	Sy 1	< 0.025	< 0.028	15.00	12	22	1
NGC 7582	23 18 23.5	-42 22 14	20.62	Sy 2	67.409 ± 3.393	77.261 ± 3.967	80.65	156 61 123	156 61 123	5
NGC 7603	23 18 56.6	+00 14 38	127.57	Sy 1.5	1.331 ± 0.070	2.639 ± 0.136	50.22	12	22	1
LCRS B232242.2-384320	23 25 24.2	-38 26 49	155.87	Sy 1	0.644 ± 0.037	1.339 ± 0.077	14.97	12	22	1

Table 1—Continued

Name	RA (J2000.0)	DEC (J2000.0)	Distance Mpc	Type	70 μ m Jy	160 μ m Jy	BAT	Aperture 70 μ m	Aperture 160 μ m	Program ID
(1)	(2)	(3)	(4)	(5)	(6)	(7)	(8)	(9)	(10)	(11)
2MASX J23272195+1524375	23 27 22.0	+15 24 37	199.97	Sy 1	0.135 ± 0.009	0.247 ± 0.024	10.52	12	22	1
NGC 7679	23 28 46.7	+03 30 41	73.35	Sy 2	8.875 ± 0.446	9.002 ± 0.458	15.12	18	22	1
IGR J23308+7120	23 30 37.7	+71 22 46	160.69	Sy 2	0.379 ± 0.028	0.810 ± 0.057	11.13	12	22	1
PKS 2331-240	23 33 55.2	-23 43 41	208.95	Sy 2	0.142 ± 0.010	0.341 ± 0.025	15.30	12	22	1
UGC 12741	23 41 55.5	+30 34 54	74.68	Sy 2	0.461 ± 0.029	1.078 ± 0.075	19.76	12	22	1

Note. — Column 1: galaxy name. Column 2-3: coordinates. Column 4: luminosity distance in Mpc. To calculate the distance we assumed a universe with a Hubble constant $H_0 = 71 \text{ km s}^{-1} \text{ Mpc}^{-1}$, $\Omega_\Lambda = 0.73$, and $\Omega_M = 0.27$, with redshift values taken from NASA’s ExtraGalactic Database (NED), except for sources with redshift values of $z < 0.01$ where distances are taken from The Extragalactic Distance Database (EDD, Tully 1988; Tully et al. 2009). Column 5: Galaxy type from Baumgartner et al. (2013), Seyfert galaxies (Sy), LINERs (L) and ESO 464-G016 (AGN, unclassified Seyfert galaxy Véron-Cetty & Véron 2010). Column 6-7: PACS flux densities. Column 8: BAT fluxes in units of $10^{-12} \text{ ergs s}^{-1} \text{ cm}^{-2}$ computed in the 14-195 keV band. Column 9-10. Aperture size in arcsec for PACS 70 μ m and 160 μ m. For elliptical apertures there are three different values, the position angle ($^\circ$) of the aperture’s major axis measured from West to North and, the minor and major diameter in arcsec. For point-like sources with flux densities fainter than $\sim 500 \text{ mJy}$ we adopted smaller apertures as recommended by the NASA Herschel Science Center. Column 11: Herschel program ID, (1) OT1_rmushotz_1, (2) OT1_lho_1, (3) GT1_msanchez_2, (4) KPGT_cwilso01_1, (5) GT1_lspinogl_2, (6) KPGT_esturm_1, (7) OT2_aalonsoh_2.

^aHigh uncertainty due to cirrus contamination in the PACS field of view

^bThere is at least one neighboring source inside the PACS field of view. In this case, we removed the neighboring source and selected an aperture that contains only the emission from the BAT source.

4. Far-Infrared Properties of the BAT sample

Figure 3 presents the histograms comparing the $70\text{ }\mu\text{m}$, $160\text{ }\mu\text{m}$ and BAT 14-195 keV luminosities of the Seyfert 1 and Seyfert 2 galaxies. We performed a Kolmogorov-Smirnov (K-S) test on the detected sources to determine whether the BAT Seyfert 1 and 2 galaxy populations are drawn from the same parent distribution. A K-S probability value of less than 5% is the probability that two samples drawn from the same parent population would differ this much 5% of the time, i.e., that they are statistically different. A strong level of significance is obtained for values smaller than 1% (e.g., Press et al. 1992; Bevington & Robinson 2003). The number of sources, mean values, standard deviations and the K-S probability of the null hypothesis for the sample are presented in Table 2. The K-S test for the luminosity distribution at $70\text{ }\mu\text{m}$ returns a 70.0% probability of the null hypothesis (i.e., the Seyfert 1 and Seyfert 2 galaxy populations are not distinguished by the present data). Similarly, the K-S null probability for the luminosity distribution at $160\text{ }\mu\text{m}$ is 52.0%. A similar situation for the Seyfert galaxies in the BAT sample has also been found in the luminosities of MIR narrow emission lines (Weaver et al. 2010) and of optical, reddening-corrected emission lines (Winter et al. 2010).

Caution must be taken when applying statistical tests to data sets that contain non-detections (upper limits), or “censored” data points. In order to deal with these problems, we used the Astronomy SURVival analysis software package ASURV Rev 1.2 (Isobe et al. 1986; Lavalley et al. 1992). We performed statistical two-sample tests and found that the luminosity distribution at $70\text{ }\mu\text{m}$ returns a 23.8% probability when using Gehan’s Generalized Wilcoxon test, in other words, two samples drawn from the same parent population would differ this much 23.8% of the time. This result is in agreement, within the statistical significance, with the K-S test on the detected sources. On the other hand, the luminosity distribution at $160\text{ }\mu\text{m}$ returns a Gehan’s Generalized Wilcoxon

test probability of 5.3%. A similar two-sample test for censored data, the Peto-Prentice generalized Wilcoxon test, returns a probability of only 4.2 % that the Seyfert 1’s and 2’s populations at 160 μm are drawn from the same parent population. Thus, the luminosity distributions of the Seyfert 1 and 2 galaxy populations at 160 μm differ at a weak but possibly statistically significant level when non-detections are included in the analysis. From this we find that Seyfert 2 galaxies have a very slightly higher mean luminosity at 160 μm , $\log L_{160\mu\text{m}} = 30.98 \pm 0.05$ ($\text{erg s}^{-1} \text{Hz}^{-1}$), than Seyfert 1 galaxies, $\log L_{160\mu\text{m}} = 30.72 \pm 0.08$ ($\text{erg s}^{-1} \text{Hz}^{-1}$). By comparison, the six sources uniquely identified as LINERs in our sample have mean luminosities at 70 and 160 μm of $\log L_{70\mu\text{m}} = 30.70 \pm 0.34$ ($\text{erg s}^{-1} \text{Hz}^{-1}$) and $\log L_{160\mu\text{m}} = 30.92 \pm 0.29$ ($\text{erg s}^{-1} \text{Hz}^{-1}$), respectively, thus different to Seyfert 1 and Seyfert 2 galaxies. The number of sources with detected and “censored” data points and the Gehan’s Generalized Wilcoxon test probability of the null hypothesis for the sample are presented in Table 2. In addition, Table 2 also shows the mean value for the entire sample of Seyfert 1 and 2 galaxies (including detections and non-detections) based on the Kaplan-Meier estimator with randomly censored data (Kaplan & Meier 1958).

The similar FIR luminosities in these two types of Seyfert galaxies implies that radiation at these wavelengths is roughly isotropic, e.g., independent of orientation. This result suggests two plausible scenarios: (i) star formation is isotropic, and hence the FIR luminosities of Seyfert 1 and 2 galaxies would be indistinguishable and/or (ii) the AGN torus is isotropic at FIR wavelengths. In the former scenario, we find that a large number of BAT sources are point-like in the PACS 70 μm images, implying a compact FIR nucleus of less than 6''(which typically encompasses regions of less than a couple of kpc). Thus, if star formation is the culprit of most of the FIR emission, then it has to happen in a very compact, nuclear region suggesting a connection between the AGN and the nuclear cold molecular gas (see Mushotzky et al. 2014). The latter scenario is in agreement with some theoretical calculations of the dusty, obscuring material surrounding the accretion disk that

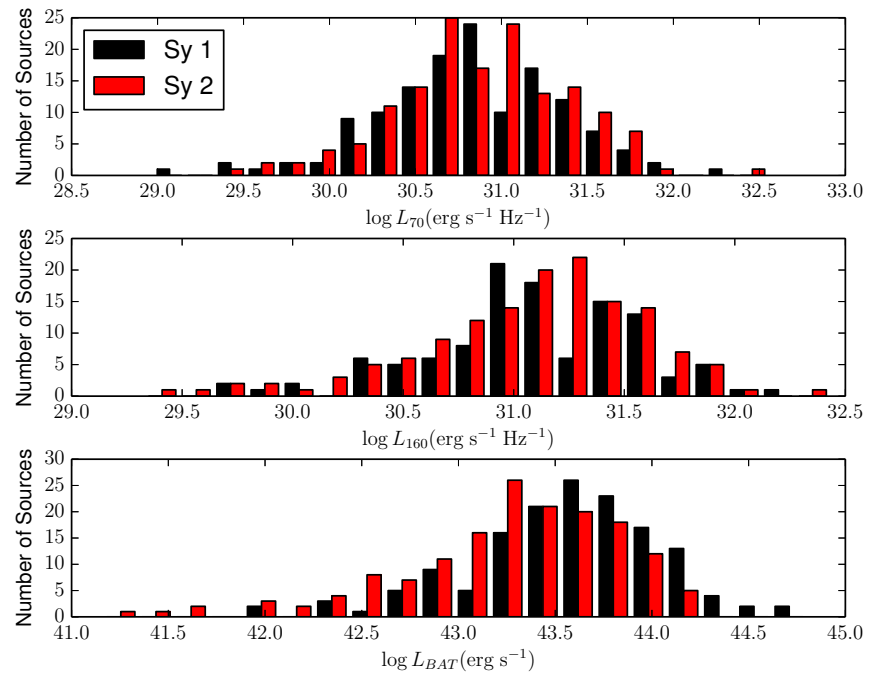


Fig. 3.— The distributions of the monochromatic luminosities for the emission at 70 and 160 μm and the integrated 14-195 keV luminosities for the sample of BAT AGN presented in this work. Upper limits are not included in the distribution.

predict a similar shape for the FIR part of the SED for both types of galaxy populations (e.g., Kennicutt et al. 2003; Stalevski et al. 2012). Note that some torus models predict an angle dependence on the FIR luminosity, with Seyfert 1 galaxies having higher luminosities than Seyfert 2 galaxies (e.g., Fritz et al. 2006). Thus, in order to match the observed FIR part of the SED, predictions from these models require an extra contribution from a circumnuclear starburst in edge-on systems. In general, much of the light would have its origin in star formation.

On the other hand, the 14-195 keV X-ray luminosities (Figure 3), bottom panel) are statistically different between the Seyfert types with a K-S test probability of $8.0 \times 10^{-3}\%$, e.g, two samples drawn from the same parent population would differ this much $8.0 \times 10^{-3}\%$ of the time. We find that Seyfert 2 galaxies have, on average, smaller luminosities, $\log L_{BAT} = 43.26 \pm 0.04$ (erg s^{-1}), than Seyfert 1 galaxies with $\log L_{BAT} = 43.57 \pm 0.05$ (erg s^{-1}), in agreement with previous results (Meléndez et al. 2008a; Winter et al. 2009; Weaver et al. 2010; Burlon et al. 2011; Ichikawa et al. 2012). This result suggests two possible scenarios: (1) Compton down scattering, even in the high energy 14-195 keV band, for some of the Seyfert 2 galaxies may be important in reducing the observed flux (e.g., Ikeda et al. 2009; Murphy & Yaqoob 2009), or (2) the statistical differences between absorbed (Seyfert 2s) and unabsorbed (Seyfert 1s) AGN are more fundamental with absorbed AGN being intrinsically less luminous than unabsorbed AGN in agreement with previous studies (e.g., Cowie et al. 2003; Steffen et al. 2003; Ueda et al. 2003; Barger et al. 2005; La Franca et al. 2005; Hasinger et al. 2005; Burlon et al. 2011). Regarding the former scenario, one must consider that there is no observational evidence of a dominant population of Compton thick (CT) AGN in the BAT survey (e.g., Burlon et al. 2011). Moreover, the fraction of CT objects in deep hard X-ray surveys has been estimated with some precision to be only $\sim 17\%$ (e.g., Bassani et al. 2013).

The latter scenario, an intrinsic difference between the luminosities of Seyfert types, is supported by the difference in the luminosity break found in the luminosity function between the two classes of objects for the BAT sample, with absorbed AGN having (on average) lower luminosities than unabsorbed AGN (e.g., Burlon et al. 2011). Overall, this scenario provides a test for the basic predictions from the unified model of AGN in which the intrinsic AGN luminosity should be independent of obscuration; that is, one must consider a model where the physical properties of the dusty, molecular torus change as a function of the intrinsic properties of the AGN central engine, e.g., accretion rate, power, etc (e.g., Lawrence 1991). For the purpose of this paper, we shall consider both scenarios as plausible and discuss their implications in the context of the FIR emission of AGN.

Table 2. Statistical Analysis for the Sample

Observable	Measurements		Mean	Standard	Measurements		Mean	Standard	<i>p</i>
	Available	(Seyfert 1)	Deviation	Available	(Seyfert 2)	Deviation			
(1)	(2)	(3)	(4)	(5)	(6)	(7)	(8)		
Statistical Analysis (censored data)									
log L _{70μm}	137	30.83	0.05	151	30.88	0.04	7.0 × 10 ⁻¹		
log L _{160μm}	113	31.08	0.04	141	31.07	0.05	5.2 × 10 ⁻¹		
log L _{BAT}	149	43.56	0.04	157	43.26	0.05	8.0 × 10 ⁻⁵		
L _{70μm} /L _{160μm}	113	0.81	0.43	139	0.77	0.47	5.4 × 10 ⁻¹		

Note. — Column 1: the observed data used for the correlation analysis. Column 2: number of Seyfert 1 galaxies used for the correlation analysis. Column 3: mean value for Seyfert 1 galaxies. Column 4: standard deviation for Seyfert 1 galaxies. Columns (5), (6) and (7) are the same as columns (2), (3) and (4) but for Seyfert 2 galaxies. Column (8): the K-S test null probability for the detected data points and Gehan's Generalised Wilcoxon test probability when upper limits are considered. In order to calculate the mean values and standard deviations with "censored" data points (number of sources with upper limits in parentheses), we used the Kaplan-Meier estimator with randomly censored data (Kaplan & Meier 1958).

^aThe mean values and standard deviations are given by the Kaplan-Meier estimator. The two-sample test

probability is given by Gehan's Generalized Wilcoxon test.

5. Far-Infrared and Hard X-ray Correlations

As we mentioned before, FIR emission is widely used as a probe of star formation. However, it is clear that if the AGN has some contribution at FIR wavelengths, then one must correct these SFR indicators accordingly. Figure 4 shows 14-195 keV luminosities versus the 70 μm or 160 μm luminosity. Due to redshift effects, luminosity–luminosity plots will almost always show some correlation. So, we used a non-parametric test for partial correlation with censored data (Akritas & Siebert 1996) in order to exclude the redshift effect. From this we find that the 14-195 keV luminosities are statistically correlated with the FIR luminosities in the Seyfert 1 galaxies with a partial Kendall $\tau_p=0.201$ and a probability of $P_\tau = 5.3 \times 10^{-6}$ at 70 μm , and $\tau_p=0.116$ and $P_\tau = 6.7 \times 10^{-3}$ at 160 μm . We find no statistically significant correlation between the 14-195 keV and FIR luminosities in the Seyfert 2 galaxies; in other words, the 14-195 keV and FIR luminosity distributions are independent (see Table 3 for details). In order to test whether these correlations are dependent on the BAT luminosity, we used the partial Kendall test in two different groups: sources with $\log L_{BAT} > 43.0$ ($\log L_{BAT} > 42.5$) and $\log L_{BAT} > 44.0$ ($\log L_{BAT} > 43.5$) for Seyfert 1 (Seyfert 2) galaxies. For Seyfert 1 galaxies at 70 μm , we find $\tau_p=0.189$ and $P_\tau = 1.6 \times 10^{-4}$ ($\log L_{BAT} > 43.0$), and $\tau_p=0.258$ and $P_\tau = 3.0 \times 10^{-2}$ ($\log L_{BAT} > 44.0$). Similarly, at 160 μm we find $\tau_p=0.117$ and $P_\tau = 1.8 \times 10^{-2}$ ($\log L_{BAT} > 43.0$), and $\tau_p=0.226$ and $P_\tau = 2.3 \times 10^{-2}$ ($\log L_{BAT} > 44.0$). Again, we find no statistically significant correlation between the 14-195 keV and FIR luminosities in the Seyfert 2 galaxies within the luminosity groups (see Table 3 for details). Note that in the Seyfert 1 galaxies the FIR-X-ray correlations get stronger for the most X-ray luminous objects suggesting that the AGN contribution overwhelms the SF contribution at high luminosities.

Table 3. Partial Correlation Analysis for the Sample

$\log X$ vs $\log Y$	τ_p	σ	P_τ	τ_p	σ	P_τ	
	(1)	(2)	(4)	(5)	(6)	(7)	
			(Seyfert 1)				
$L_{BAT} - L_{70}$	0.201	0.044	5.3×10^{-6}	0.076	0.041	6.4×10^{-2}	
$L_{BAT} - L_{160}$	0.116	0.043	6.7×10^{-3}	-0.005	0.042	9.1×10^{-1}	
			$\log L_{BAT} > 43.0$				
$L_{BAT} - L_{70}$	0.189	0.050	1.6×10^{-4}	0.063	0.045	1.6×10^{-1}	
$L_{BAT} - L_{160}$	0.117	0.049	1.8×10^{-2}	-0.007	0.046	8.7×10^{-1}	
			$\log L_{BAT} > 44.0$				
$L_{BAT} - L_{70}$	0.258	0.119	3.0×10^{-2}	0.004	0.090	9.6×10^{-1}	
$L_{BAT} - L_{160}$	0.226	0.100	2.3×10^{-2}	0.009	0.096	9.2×10^{-1}	
W/O CT							
$L_{BAT} - L_{70}$				0.065	0.043	1.2×10^{-1}	
$L_{BAT} - L_{160}$				-0.014	0.044	7.5×10^{-1}	
W/O CT and Candidates for CT							
$L_{BAT} - L_{70}$				0.084	0.048	8.0×10^{-2}	
$L_{BAT} - L_{160}$				-0.019	0.049	9.6×10^{-1}	

Note. — Column 1: $\log X$ and $\log Y$ represent the independent and dependent variables, respectively. Column 2: τ_p is the Kendall's coefficient for partial correlation with censored data for Seyfert 1 galaxies. Column 3: σ is the calculated variance for Seyfert 1 galaxies. Column 4: P_τ is the associated null probability for Kendall τ_p for Seyfert 1 galaxies. Columns (5), (6) and (7) are the same as columns (2), (3) and (4) but for Seyfert 2 galaxies. We also show the correlation analysis for the sample of Seyfert 2 galaxies when Compton Thick (CT, Table 5) sources are excluded (W/O CT) and, when CT and candidates for CT are excluded (W/O CT and Candidates for CT, see Table 5 and 6).

Overall, for the Seyfert 1 galaxies, we find a better correlation at 70 μm than at 160 μm . This result is in agreement with previous works where the correlations between 14-195 keV luminosities and different monochromatic infrared luminosities get weaker at longer wavelengths where the contribution from star formation might be greater. For example, the tightest and most significant correlations are found between the 14-195 keV luminosities and the 9,12 and 18 μm emission (e.g., Gandhi et al. 2009; Matsuta et al. 2012; Ichikawa et al. 2012), and the correlations get less significant at longer FIR wavelengths (e.g., Meléndez et al. 2008b; Nenkova et al. 2008b; Matsuta et al. 2012; Ichikawa et al. 2012). However, this is the first time that a weak but possibly statistically significant correlation between the intrinsic power of the AGN and the FIR emission at 160 μm has been found. These results suggest two possible scenarios: (1) if we assume that the FIR luminosity is a good tracer of star formation (e.g., Calzetti et al. 2010), then there is a connection between star formation and the AGN at sub-kiloparsec scales (e.g., Mushotzky et al. 2014), or (2) dust heated by the AGN has a statistically significant contribution to the FIR emission at 70 and 160 μm . In the latter scenario, SFR indicators that rely on FIR emission, either through the individual infrared bands (Calzetti et al. 2010) or the total FIR emission (8–1000 μm , Kennicutt 1998), need to consider the AGN contribution in their predictions. Note that in order to increase the FIR emission predicted from the outer (and colder) regions of many torus models (AGN contribution), one could use any combination of free parameters, such as an increase of the torus radius with a constant optical depth, a flatter radial density profile and/or an edge-on orientation (e.g., Nenkova et al. 2008b; Stalevski et al. 2012). Within these parameters (uncertainties), smooth, continuous torus models seem to be able to predict higher FIR fluxes than clumpy torus calculations (with a broader range of SED shapes); however, clumpy models provide a better match to the MIR portion of the SED (e.g., Mullaney et al. 2011).

In addition, Figure 4 shows different linear regression methods applied to the sample

(see Table 4 for values). In order to test the effect of the upper limits in our sample, we estimated the linear regression coefficients using the EM (expectation-maximization) algorithm with censored data (Isobe et al. 1986) and an ordinary least-square regression of the dependent variable, Y, against the independent variable X, (OLS) without the inclusion of censored data (only detections). Both methods show a good agreement, within their uncertainties, suggesting that the non-detections in our sample do not significantly change the results. However, it is not clear that the FIR luminosity is a direct consequence of the BAT luminosity; thus, a bisector method may be more appropriate to investigate the underlying functional relationship between the hard X-ray and FIR luminosities (Isobe et al. 1990). From this we find a nearly linear relationship between the AGN and PACS monochromatic luminosities, with Seyfert 1 and Seyfert 2 galaxies having similar slopes within the given uncertainties. Overall, these values are in agreement with the slopes found by Matsuta et al. (2012) between the 14-195 keV and 90 μm luminosities.

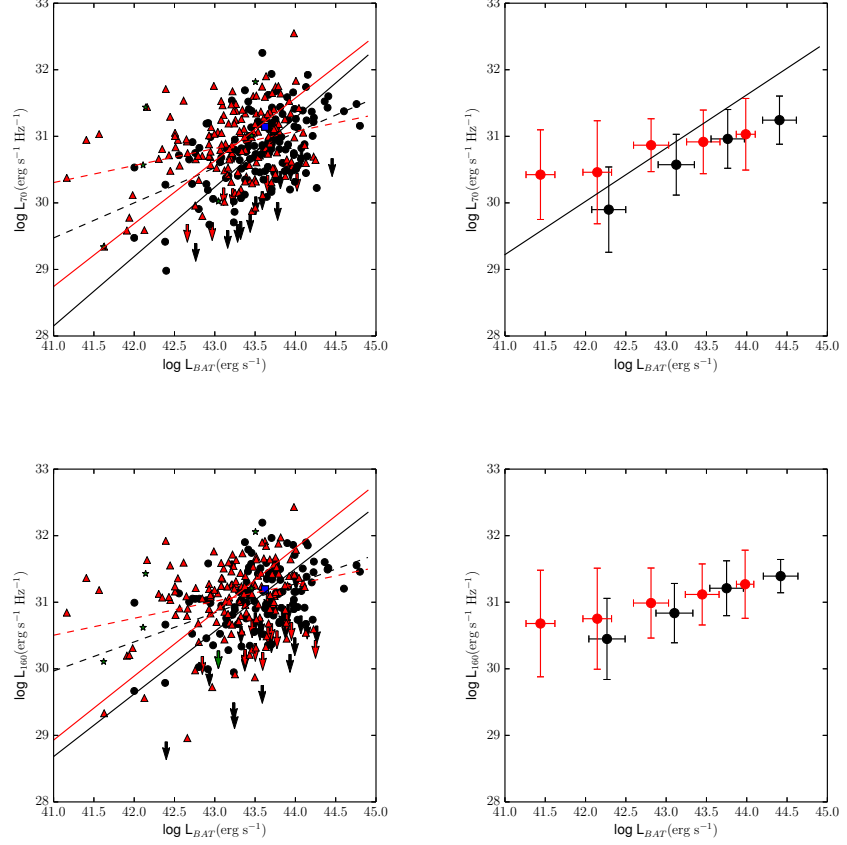


Fig. 4.— Left panel: correlation between the monochromatic luminosities at 70 and 160 μm and the 14-195 keV luminosity (L_{BAT}) in Seyfert 1 (black circles), Seyfert 2 (red triangles), LINERs (green stars) and AGN (blue square). AGN refers to unidentified or previously unknown AGN. The dashed and solid lines represent the linear regression using the OLS and bisector methods, respectively, separated into Seyfert 1 (black lines) and Seyfert 2 (red lines) galaxies. Right panel: binned correlation between the monochromatic luminosity at 70 and 160 μm and the 14-195 keV luminosity in Seyfert 1 (black) and Seyfert 2 (red) galaxies. We choose 5 equally spaced bins within the range of the FIR monochromatic and BAT luminosities. The error bars are the standard deviations for each quantity. The solid line in the upper right panel is the AGN dominated line from Netzer (2009) (see text for details).

Table 4. Linear regressions for the Far-infrared and the 14–195 keV Luminosities

$\log X$ vs $\log Y$	$\log Y = m \log X + b^1$		$\log Y = m \log X + b^1$		$\log Y = m \log X + b^1$	
	m	b	m	b	m	b
	(1)	(2)		(3)		(4)
Seyfert 1 Galaxies:						
$L_{\text{BAT}} - L_{70}$	0.54 ± 0.09	7.45 ± 3.79	0.52 ± 0.08	8.14 ± 3.70	1.04 ± 0.07	-14.60 ± 2.87
$L_{\text{BAT}} - L_{160}$	0.45 ± 0.11	11.06 ± 4.74	0.44 ± 0.08	11.95 ± 3.51	0.94 ± 0.06	-9.88 ± 2.74
Seyfert 2 Galaxies:						
$L_{\text{BAT}} - L_{70}$	0.26 ± 0.07	19.83 ± 3.22	0.25 ± 0.08	20.13 ± 3.64	0.94 ± 0.04	-9.96 ± 1.84
$L_{\text{BAT}} - L_{160}$	0.13 ± 0.08	25.30 ± 3.33	0.25 ± 0.09	20.32 ± 4.06	0.96 ± 0.05	-10.52 ± 2.09

¹m and b represent the regression coefficient (slope) and regression constant (intercept), respectively.

Note. — Column 1: $\log X$ and $\log Y$ represent the independent and dependent variables, respectively. Column 2: linear regression coefficients using the EM algorithm with censored data (upper limits). Column 3: ordinary least-square regression of the dependent variable, Y, against the independent variable X, OLS(Y—X) without the inclusion of censored data. Column 4: OLS bisector method without censored data which treat the variables symmetrically. See Isobe et al. (1990) for a review of all the methods.

Included as well in Figure 4 is the relation between L_{60} and L_{bol} for AGN dominated sources from Netzer (2009) (black line in upper right panel). In order to compare this relation with our sample, we assumed a mean ratio of $S_{70}/S_{60} = 1.09$, as derived from the PACS-IRAS comparison presented in Figure 2, and a constant ratio of 10.5 to transfer the 14-195 keV luminosity to bolometric luminosity (Winter et al. 2012). Overall, the Netzer (2009) relationship for AGN dominated sources is in fair agreement with the mean values of our sample, and it extends linearly over our range of X-ray luminosities. Note that systems above this straight line may be dominated by star formation in the host galaxy resulting in the flatter slope observed in Seyfert 2 galaxies at low BAT luminosities, $\log L_{BAT} < \sim 42.5$ erg s $^{-1}$ (or $\log L_{bol} < \sim 43.7$ erg s $^{-1}$). This luminosity is smaller, by a factor of ~ 3 , than the turnover value found by Rosario et al. (2012) for local AGN, $\log L_{bol} = 44.23 \pm 0.13$ (erg s $^{-1}$), however, Seyfert 1 galaxies show no turnover over our range of X-ray luminosities. Netzer (2009) suggested a time evolution scenario to explain the L_{60} versus L_{bol} linear correlation, where the galaxy transitions from a pure starburst to a powerful composite starburst-AGN and, finally, to a weak composite starburst-AGN phase. In this scenario, after a long star formation period, some of the cold gas is funneled to the center of the galaxy and feeds the black hole, resulting in a short period of intense AGN and stellar activity with high star formation and accretion rate. This stage is characterized by sources rising and moving horizontally above the straight line in the right upper panel in Figure 4. As the cold gas supply diminishes, both the star formation and the central AGN fade in parallel and fall below the straight line (see Figure 14 in Netzer 2009). Interestingly, this scenario may suggest an analogous evolutionary connection between the Seyfert 1 and Seyfert 2 branches in our L_{70} versus L_{BAT} comparison. Here Seyfert 2 galaxies, dominated by star formation, are above the straight line. As they evolve in time, they reach their maximum AGN and star formation activity until the Seyfert 1 and Seyfert 2 galaxy branches grow together at high star formation, L_{70} , and AGN luminosity, L_{BAT} . As the

supply of cold gas is reduced, the AGN and star formation luminosity fade together below the straight line, evolving into the observed Seyfert 1 galaxy branch. Note that the slope of the Netzer (2009) relationship ($L_{60} \propto L_{bol}^{0.8}$) is in good agreement with our values derived from the bisector method whereas the OLS slopes are much flatter.

5.1. Seyfert 2 Galaxies

In the previous section, we proposed two scenarios to explain the statistical differences in the 14-195 keV luminosity distribution between Seyfert 1 and Seyfert 2 galaxies: the effect of Compton scattering in the Seyfert 2 population, or that Seyfert 2 galaxies are intrinsically less luminous than Seyfert 1 galaxies. In the following discussion, we will investigate the effect of these scenarios in the FIR and hard X-ray relationship in order to find the culprit for the lack of correlation between the 14-195 keV and FIR luminosities in Seyfert 2 galaxies. In the former scenario, if Compton scattering in the 14-195 keV band is important, then the more heavily obscured sources are responsible for breaking the intrinsic correlation between the FIR and the hard X-ray by reducing the X-ray flux and, perhaps, increasing the FIR emission. This scenario is in agreement with the lack of a correlation found between the 14-195 keV luminosities and the *AKARI* infrared luminosities at 90 μ m in CT AGN for the the 22-month BAT survey (Matsuta et al. 2012). Moreover, in this sample, Seyfert 2 galaxies are correlated if CT AGN are excluded. In order to test the effect of high X-ray column densities on the FIR and X-ray correlations, we have compiled published values for the X-ray column densities of Seyfert 2 galaxies in our sample (see Tueller et al. 2008; Winter et al. 2009; Burlon et al. 2011; Vasudevan et al. 2013, and references therein). From this we found that 106 out of 157 Seyfert 2 galaxies have published X-ray column densities with 18 sources having high X-ray column densities, $N_H > 10^{24}$ cm $^{-2}$ (see Table 5). We use the same partial correlation analysis as before and

find that, even when excluding the CT sources presented in Table 5, there is no statistically significant correlation between the 14-195 keV and FIR luminosities (70 and 160 μm) in Seyfert 2 galaxies when the influence of distance is excluded (see Table 3).

As we mentioned before, the fraction of CT AGN in deep hard X-ray surveys is $17\% \pm 3\%$ (Bassani et al. 2013). This fraction of CT AGN is in agreement with the value derived from the northern Galactic cap of the 58-month BAT catalog, where they found that up to 15% of their sample could be CT (Vasudevan et al. 2013). Since we identified only 18 CT candidates in our sample, this suggests that there may be some heavily obscured Seyfert 2 galaxies that are unaccounted for. In order to have an estimate of the X-ray column density for the sources without published values (51 out of 157), we used a simple color-color diagram initially presented in Winter et al. (2008), and later in Winter et al. (2009). Figure 5 shows the soft/medium (0.5-2 keV flux/2-10 keV flux) and the hard/medium (14-195 keV flux/2-10 keV flux) ratios for the 51 Seyfert 2 galaxies without published X-ray column densities. Fluxes for the soft (0.5-2 keV) and medium (2-10 keV) X-ray were taken from the seven year *Swift*-XRT point source catalog (D’Elia et al. 2013). In the diagram we also show the position for the CT sources in our sample (open red triangles-circles). It is clear from this comparison that our CT sources are located in the same branch of heavily obscured sources $N_{\text{H}} > 10^{23} \text{ cm}^{-2}$ which extends towards the upper right side of the diagram (see Figure 3 in Winter et al. 2009). We find that the vast majority of the CT sources have hard/medium flux ratios, $14\text{-}195 \text{ keV flux}/2\text{-}10 \text{ keV flux} > 10$; thus this is a simple approximation for identifying heavily obscured or CT candidates. We apply this criteria to identify heavily obscured sources from our sample of Seyfert 2 galaxies, in particular, those sources without published column densities. Overall, we find 26 sources with hard/medium ratios greater than ~ 10 , indicative of high column densities (see Table 6 for details). We performed a partial correlation analysis in our Seyfert 2 population after excluding the CT sources (Table 5) and our candidates of heavily obscured Seyfert 2 galaxies without

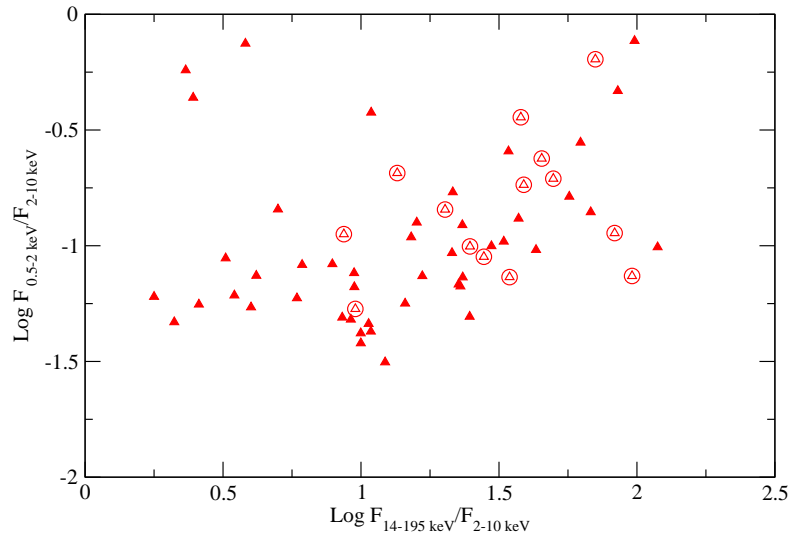


Fig. 5.— Color-color diagram for the Seyfert 2 galaxies in our sample without published X-ray column density values (solid red triangles). Fluxes for the soft (0.5-2 keV) and medium (2-10 keV) X-ray were taken from the seven year *Swift*-XRT point source catalog (D'Elia et al. 2013). For comparison, we identified the Compton Thick sources (Table 5) as open red triangles-circles.

published X-ray column densities (Table 6). We find that there is no statistically significant correlation between the 14-195 keV and FIR luminosities (70 and 160 μm) in Seyfert 2 galaxies when the influence of distance is excluded (see Table3). These results suggest that Compton scattering in the BAT band is not responsible for the lack of a correlation between the hard X-ray and FIR luminosities.

Table 5. Properties of Compton thick or heavily obscured Seyfert 2 galaxies,

$$N_H > 10^{24} \text{cm}^{-2}$$

Name	N_H 10^{24}cm^{-2}	Reference
(1)	(2)	(3)
CGCG 420-015	1.46	(1)
ESO 005-G004	1.01	(2)
ESO 137-G034	> 1.5	(3)
MCG-01-30-041	1.45	(4)
Mrk 3	1.36	(5)
Mrk 417	1.20	(4)
NGC 424	1.00	(6)
NGC 1365	4.00	(7)
NGC 3079	5.40	(6)
NGC 3281	2.00	(8)
NGC 3393	4.50	(6)
NGC 4939	>10.00	(9)
NGC 4941	1.32	(4)
NGC 5728	1.39	(10)
NGC 6240	1.83	(6)
NGC 6552	>1.00	(11)
NGC 7582	1.10	(6)
UGC 05881	2.45	(4)

Note. — Column 1: galaxy name.
Column 2: X-ray absorbing column density. Column 3: references for the column density. (1) Severgnini et al. (2011); (2) Ueda et al. (2007); (3) Malizia et al. (2009); (4) Vasudevan et al. (2013); (5) Bianchi et al. (2005); (6) (Burlon et al. 2011); (7) Risaliti et al. (2009); (8) Vignali & Comastri

(2002); (9) Maiolino et al. (1998); (10)
Comastri et al. (2010); (11) Bassani et al.
(1999)

On the other hand, if Seyfert 2 galaxies are intrinsically less luminous than Seyfert 1 galaxies, then the lack of a correlation suggests that the FIR-X-ray connection is luminosity dependent. In this scenario, low luminosity AGN show little or no relationship between the AGN and the FIR luminosity, because the latter is dominated by dust heated primarily by the stellar activity in the host galaxy (e.g., Rosario et al. 2012). At higher luminosities (where the AGN dominate), dust heated by the AGN becomes non-negligible, thereby, creating the correlation between the intrinsic power of the AGN and the FIR (e.g., Netzer 2009; Rosario et al. 2012).

Table 6. Candidates for Compton thick or heavily obscured Seyfert 2 galaxies,

$$N_H > 10^{23} \text{ cm}^{-2}$$

Name (1)	$F_{14-195\text{keV}}/F_{2-10\text{keV}}$ (2)	$F_{0.5-2\text{keV}}/F_{2-10\text{keV}}$ (3)
2MASX J01064523+0638015	10.66	0.05
2MASX J01073963-1139117	22.57	0.07
2MASX J04234080+0408017	32.92	0.10
2MASX J06411806+3249313	10.86	0.04
2MASX J06561197-4919499	56.87	0.16
2MASX J07262635-3554214	21.36	0.09
2MASX J09360622-6548336	15.92	0.13
2MASX J20101740+4800214	24.76	0.05
2MFGC 02280	118.83	0.10
CGCG 102-048	43.07	0.10
CGCG 312-012	16.68	0.07
ESO 244-IG030	21.50	0.17
ESO 374-G044	14.45	0.06
ESO 439-G009	34.23	0.26
ESO 565-G019	23.37	0.07
II Zw 083	15.20	0.11
MCG-07-03-007	68.01	0.14
MCG+02-21-013	29.70	0.10
MCG+06-16-028	85.26	0.47
MCG+06-49-019	10.88	0.38
MCG+11-11-032	12.23	0.03
NGC 1106	98.05	0.77
NGC 1125	62.47	0.28
SBS 0915+556	23.30	0.12
UGC 01479	22.92	0.07
VII Zw 073	37.26	0.13

Note. — Column 1: galaxy name. Column 2: the soft/medium (0.5-2 keV flux/2-10 keV flux). Column 3: the hard/medium (14-195 keV flux/2-10 keV flux). Fluxes for the soft (0.5-2 keV) and medium (2-10 keV) X-ray were taken from the seven year *Swift*-XRT point source catalog (D'Elia et al. 2013)

6. The Far-Infrared Colors of the BAT sample

Typically, FIR emission from galaxies peaks between ~ 100 - 160 μm . Thus, the F_{70}/F_{100} versus F_{100}/F_{160} can be used to trace the peak of the galaxy SED (e.g., Rémy-Ruyer et al. 2013). However, in the absence of 100 μm observations the F_{70}/F_{160} ratio may still provide useful information regarding the peak of the FIR SED and the dust properties. Figure 6 shows the distribution of this ratios for between Seyfert 1 and Seyfert 2 galaxies in the BAT sample. The K-S test null probability is 53.5% which indicates that the two galaxy populations have similar FIR colors, in agreement with the statistical similarities between the monochromatic luminosities at 70 and 160 μm (see Table 2).

Figure 7 shows the F_{70}/F_{160} ratio versus the intrinsic X-ray luminosity of the AGN. We find a trend of increasing F_{70}/F_{160} with BAT luminosity. Our analysis reveals a weak but statistically significant correlation with a generalized Spearman rank-order correlation coefficient and probability (with censored data), $\rho = 0.174$, $P_\rho = 4.3 \times 10^{-2}$ for Seyfert 1 galaxies and a similar correlation for Seyfert 2 galaxies with $\rho = 0.236$, $P_\rho = 3.9 \times 10^{-3}$. This result implies that there may be a dust grain distribution with a warm (nuclear) dust component, heated by the very energetic environment in the proximity of the AGN (with a strong contribution to the 70 μm continuum), and a colder dust component farther out in the outer regions of the AGN torus and/or the host galaxy (the primary contributor to the 160 μm continuum). In order to investigate the AGN contribution to the FIR colors, we compared our observed colors with predictions from three different torus models: the smooth, continuous torus from Fritz et al. (2006)⁷ and the clumpy torus models from Hönig & Kishimoto (2010)⁸ and Stalevski et al. (2012) (“smooth”, “two-phase” and

⁷<http://users.ugent.be/~jfritz/jfhp/TORUS.html>

⁸<http://www.sungraizer.org/CAT3D.html>

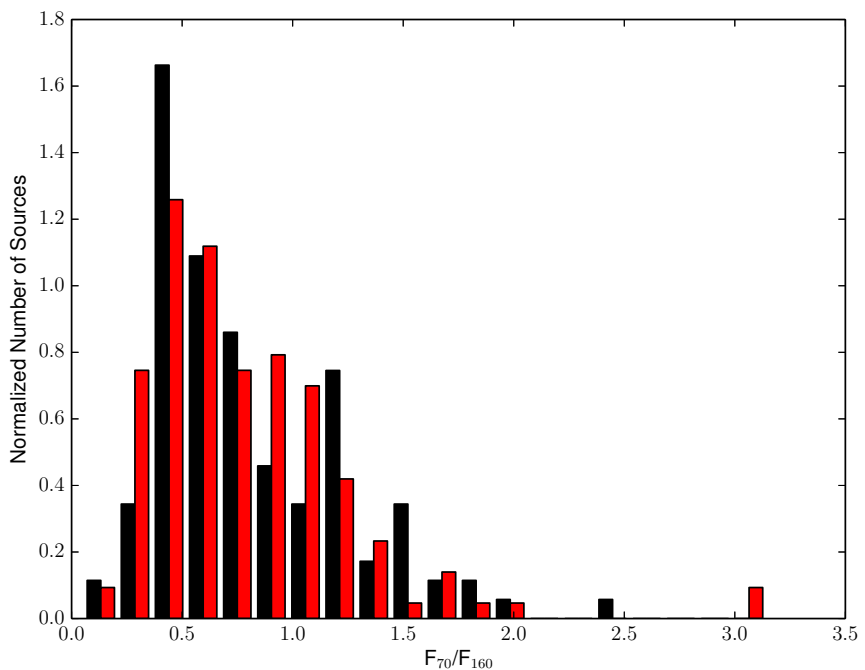


Fig. 6.— The distribution of the F_{70}/F_{160} ratio for Seyfert 1 and Seyfert 2 galaxies. The legend is the same as in Figure 3. Upper limits are not included in the distribution.

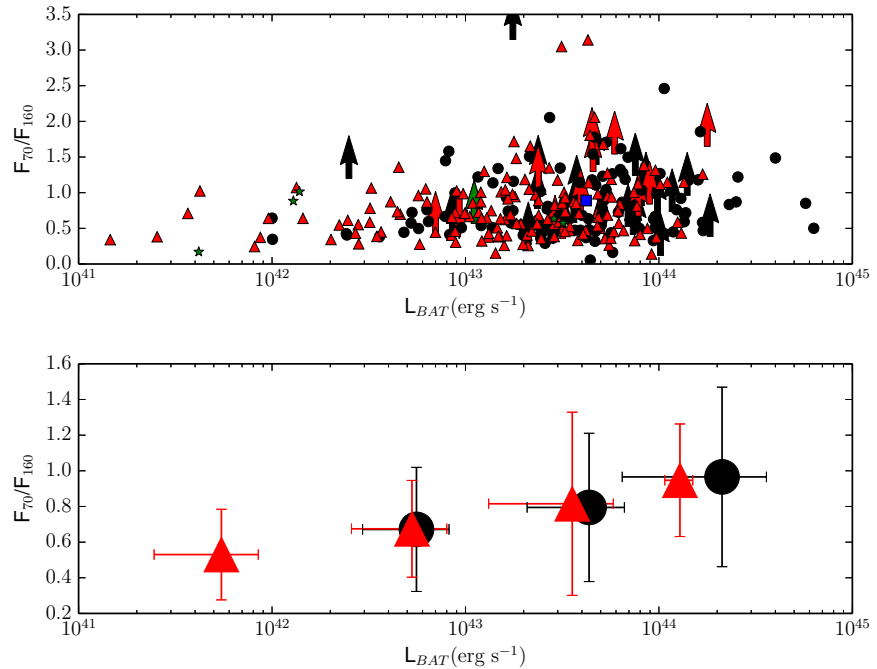


Fig. 7.— Upper panel: correlation between the FIR color, F_{70}/F_{160} , and the 14-195 keV luminosity (L_{BAT}). Lower panel: binned correlation between the FIR color, F_{70}/F_{160} , and the 14-195 keV luminosity (L_{BAT}). We choose 4 equally spaced bins within the range of the 14-195 keV luminosity. Symbols are: Seyfert 1 (black circles), Seyfert 2 (red triangles), LINERs (green stars) and AGN (blue square)

“clumps-only”)⁹. We find that there is no region in parameter space (input parameters for the different models) that can reproduce F_{70}/F_{160} ratios less than unity. In addition, the vast majority of the BAT AGN (74% of all the sources with detections in both FIR bands) have F_{70}/F_{160} ratios less than unity.

All these models, on average, overpredict the F_{70}/F_{160} ratios by at least a factor of 2-3 (Fritz et al. 2006; Hönig & Kishimoto 2010) and as much as a factor of ~ 20 (Fritz et al. 2006; Stalevski et al. 2012) (see Figure 8). Continuous models with a torus full-opening angle of $\Theta = 60^\circ$ (covering factor, Fritz et al. 2006) can reproduce the most extreme sources in our sample at the high end of the observed FIR color distribution with $F_{70}/F_{160} > \sim 2.5$, namely Mrk 841, MCG-05-23-016 and ESO 103-035. Note that the observed BAT FIR SED is the combined effect from the AGN (non-thermal) and a stellar (thermal) radiation field. Therefore, it is not unexpected for the torus models to underpredict the observed FIR part of the SED without an extra stellar component (see discussion in Section 4). However, the weak but probably statistically significant correlation between the intrinsic power of the AGN and the FIR emission in Seyfert 1 galaxies suggests that there is a subset of the BAT AGN in which the FIR emission is dominated by the non-stellar contribution (AGN). This population includes AGN dominated sources with weak or no signatures of star formation at other wavelengths (e.g., Hönig et al. 2014). Therefore, the previous results suggest that current torus models may underpredict the intrinsic AGN emission at 160 μm , relative to the 70 μm , by having a steeper FIR SED.

⁹<https://sites.google.com/site/skirtorus/home>

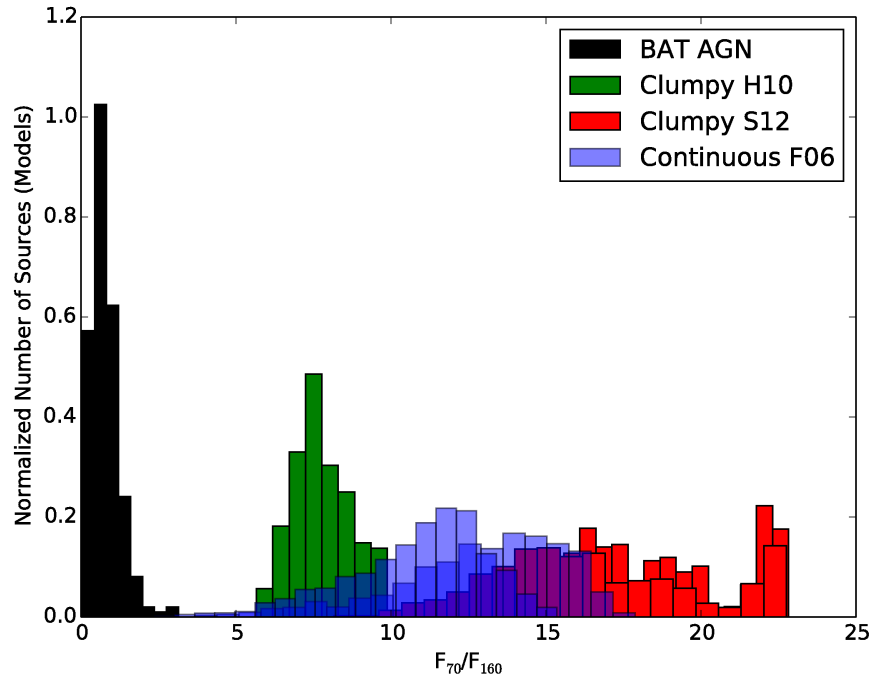


Fig. 8.— A comparison between the observed distribution of the FIR colors, F_{70}/F_{160} , for the BAT sample and predictions from different torus models. A smooth, continuous torus model from Fritz et al. (2006) (F06) for two different torus opening angles, $\Theta = 140^\circ$ and $\Theta = 60^\circ$. Clumpy torus models from Höning & Kishimoto (2010) (H10) and Stalevski et al. (2012) (S12) with a combination of “smooth”, “two-phase” and “clumps-only” models. For the sake of simplicity, we combined, within each torus model, all the predictions from different input parameters. The histogram is normalized by unit of area.

7. Comparison with Normal Galaxies

The F_{70}/F_{160} ratio provides useful information when comparing with other samples of galaxies. Figure 9 shows the F_{70}/F_{160} distribution between the BAT AGN, the Key Insights on Nearby Galaxies: a Far-Infrared Survey with Herschel (KINGFISH) sample of nearby galaxies (Dale et al. 2012) and the dwarf galaxy survey (DGS) (Rémy-Ruyer et al. 2013). The KINGFISH sample is an imaging and spectroscopic survey of 61 nearby ($d < 30$ Mpc) galaxies draw mainly from the Spitzer Infrared Nearby Galaxies Survey (SINGS; see Kennicutt et al. 2003, for details). The KINGFISH sample covers a wide range of galaxy properties and local interstellar medium environments found in the nearby Universe. The *Herschel* DGS is a photometric and spectroscopic sample of dwarf galaxies in the local universe chosen to cover a wide range of physical conditions, including a wide range of metallicities (Madden et al. 2013).

For the KINGFISH sample, we selected only the “normal” galaxies, e.g., the non-AGN galaxies as classified by their optical spectra (Moustakas et al. 2010). Conversely, for the comparison we included all BAT AGN. From Figure 9 it is clear that the BAT AGN and the KINGFISH normal galaxies span a similar range of values with a K-S null probability of 31%, in other words, the BAT AGN FIR colors are statistically indistinguishable from those in normal galaxies. On the other hand, the FIR colors for the BAT AGN are statistically different than those in the DGS sample with a K-S test null probability of 0.0 %. The majority of the BAT AGN and KINGFISH galaxies have $F_{70} < F_{160}$ corresponding to colder dust, whereas most of the dwarf galaxies peak at shorter wavelengths, $F_{70}/F_{160} > 1$, suggesting a warmer dust due to the harder radiation field illuminating the environment surrounding young stars. Note that F_{70}/F_{160} is also sensitive to metallicity, in that the lower metallicity galaxies have warmer dust than that found in their metal-rich counterparts (Rémy-Ruyer et al. 2013).

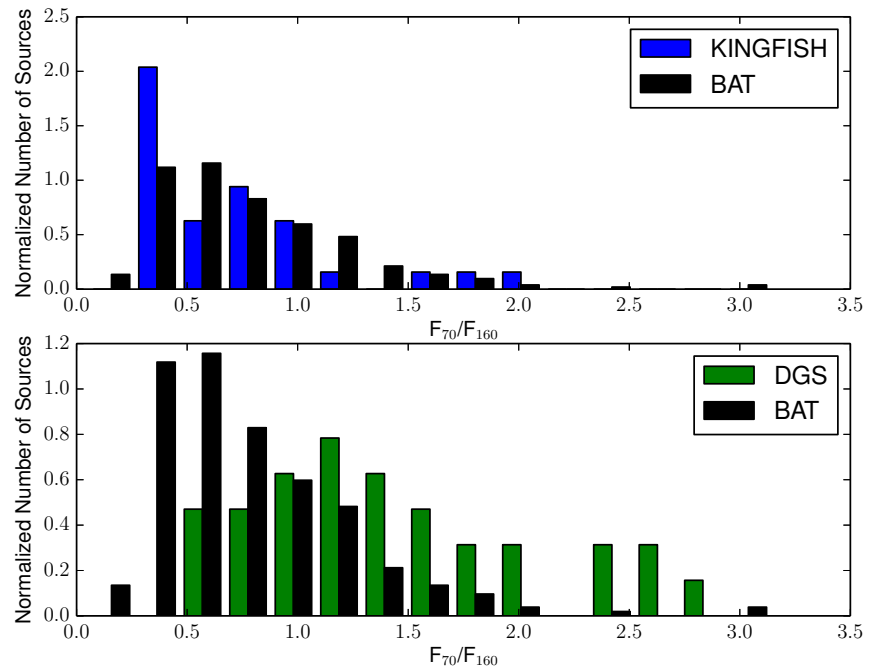


Fig. 9.— A comparison between the distributions of the F_{70}/F_{160} ratios for the entire BAT sample with the KINGFISH sample (upper panel) and the dwarf galaxy survey DGS (lower panel). The histograms are normalized by unit of area.

8. Conclusions

We present FIR flux densities and maps for 313 hard X-ray selected AGN from the low-redshift ($z < 0.05$) 58-month Swift-BAT survey in two PACS bands at 70 and 160 μm . Of the 313 sources, 94% and 83% are detected in the FIR by PACS at 70 and 160 μm , respectively. From our analysis we find the following:

(1) Using the K-S test the FIR luminosity distributions at 70 and 160 μm for the Seyfert 1 and Seyfert 2 galaxies are indistinguishable from one another. This result suggests that the FIR emission is isotropic, e.g., independent of orientation. We propose two different interpretations for the isotropic nature of the FIR emission: (i) star formation, which is isotropic, and/or (ii) some AGN torus models predict isotropy at FIR wavelengths. Regarding the former scenario, if star formation dominates the FIR emission, then it has to happen in a very compact, nuclear region, suggesting a connection between the AGN and the nuclear cold molecular gas (see Mushotzky et al. 2014). In the latter scenario, torus models predict a similar shape for the FIR part of the SED for both types of Seyferts (e.g., Kennicutt et al. 2003; Stalevski et al. 2012). However, some torus models predict an angle dependence on the FIR luminosity with Seyfert 1 galaxies having higher luminosities than Seyfert 2 galaxies. For these models, star formation would also be needed (e.g., Fritz et al. 2006)

Using the two-sample test for censored data, the 160 μm luminosity distributions between Seyfert galaxies may be distinguishable at a weak but possibly statistically significant level. By including the non-detections, the Seyfert 2 galaxies are found to have a very slightly higher mean luminosity than the Seyfert 1 galaxies. If the FIR emission is a good probe of star formation, then this result suggests that Seyfert 2 galaxies have a slightly higher SFR than Seyfert 1 galaxies, which could imply a time-dependent evolutionary scenario, where the AGN are more obscured when the SFRs are at their higher values (see

discussion in Section 5).

(2) A K-S test on the present data shows that the 14-195 keV luminosity distributions are statistically different between Seyfert 1 (unabsorbed) and Seyfert 2 (absorbed) galaxies. Our analysis suggests that the statistical differences between AGN types are fundamental, with absorbed AGN intrinsically less luminous than unabsorbed AGN. This scenario is supported by the difference in the luminosity function between the two types of Seyferts for the BAT sample, with absorbed AGN having, on average, lower luminosities than unabsorbed AGN (e.g., Cowie et al. 2003; Steffen et al. 2003; Ueda et al. 2003; Barger et al. 2005; La Franca et al. 2005; Hasinger et al. 2005; Burlon et al. 2011). Overall, this is a challenge for the basic predictions from the unified model of AGN, where the intrinsic AGN luminosity should be independent of obscuration. Thus, one must consider a luminosity-dependent unified model of AGN (e.g., Barger et al. 2005).

(3) Using a non-parametric test for partial correlation with censored data, we find a statistically significant correlation between the AGN intrinsic power (BAT luminosity) and the FIR emission at 70 and 160 μm in Seyfert 1 galaxies. We find a better correlation between the BAT and PACS luminosities at 70 μm than at 160 μm . The correlation is also stronger for the most X-ray luminous objects. The observed correlations suggest two possible scenarios: (i) if we assume that the FIR luminosity is a good tracer of star formation, then there is a connection between star formation and the AGN at sub-kiloparsec scales, and/or (ii) dust heated by the AGN has a statistically significant contribution to the FIR emission. Regarding the former scenario, and given the fact that the majority of the BAT sources have their FIR fluxes dominated by a point source located at the nucleus, one needs to consider that star formation has to happen in a very compact, nuclear region (Mushotzky et al. 2014). In the latter, SFR indicators that rely on FIR emission, either through the individual infrared bands (Calzetti et al. 2010) or the total FIR emission

(8–1000 μm , Kennicutt 1998), need to consider the AGN contribution in their predictions. However, all torus models studied in the present work underpredict the amount of cold dust (from the outer regions of the torus) needed to match the observations; thus, a stellar component may still be required.

(4) A non-parametric test for partial correlation with censored data reveals that there is no statistically significant correlation between the 14–195 keV and FIR luminosities in Seyfert 2 galaxies when the influence of the distance is excluded. The results presented in this paper support a scenario in which Seyfert 2 galaxies are intrinsically less luminous than Seyfert 1 galaxies suggesting that the FIR-X-ray connection is luminosity dependent. In other words, in low luminosity AGN (Seyfert 2 galaxies), the FIR may be dominated by dust heated primarily by the stellar activity in the host galaxy (e.g., Rosario et al. 2012), while at higher luminosities (Seyfert 1 galaxies) the contribution from dust heated by the AGN overwhelms the star formation contribution, thereby, creating the correlation between the intrinsic power of the AGN and the FIR.

(5) Using a K-S test, the distributions of the F_{70}/F_{160} ratios for the Seyfert 1 and 2 galaxies are indistinguishable from one another. They are also indistinguishable from those of normal star forming galaxies. In general, we find that the vast majority of the BAT AGN (74% of all sources with a detection in both FIR bands) have F_{70}/F_{160} ratios less than unity. Assuming that the FIR is dominated by star formation, these results are in agreement with the isotropic nature of the star formation emission. However, one must consider that the weak but statistically significant correlation between the intrinsic power of the AGN and the FIR emission suggests that there must be an underlying population of BAT AGN in which the FIR emission is dominated by the non-stellar contribution (the AGN torus). This population includes AGN dominated sources with weak or no signatures of star formation at other wavelengths, e.g., Mrk 3 (e.g., Sales et al. 2014). Nonetheless, when comparing

with predictions from different torus models, we find that there is no region in parameter space (input parameters for the different models) that can reproduce F_{70}/F_{160} ratios less than unity. All these models, on average, overpredict the F_{70}/F_{160} ratios by at least a factor of 2-3 (Fritz et al. 2006; Hönig & Kishimoto 2010) and by as much as a factor of ~ 20 (Fritz et al. 2006; Stalevski et al. 2012). Continuous models with a torus full-opening angle of $\Theta = 60^\circ$ (covering factor, Fritz et al. 2006) can only reproduce the most extreme sources at the high end of the observed FIR colors distribution with $F_{70}/F_{160} > \sim 2.5$, namely Mrk 841, MCG-05-23-016 and ESO 103-035. Thus, current torus models may underpredict the AGN emission at $160\text{ }\mu\text{m}$ (colder dust) relative to $70\text{ }\mu\text{m}$ with a steeper FIR SED.

(6) Using a Spearman rank-order analysis, the 14-195 keV luminosities for the Seyfert 1 and 2 galaxies are weakly statistically correlated with the F_{70}/F_{160} ratios. This result suggests two possible interpretations: (i) a time-evolutionary sequence, as discussed in Section 5, where SFRs are higher in the more X-ray luminous sources, producing a trend of increasing AGN luminosity and FIR temperature, and/or (ii) the existence of a dust grain distribution with a warm (nuclear) dust component, heated by the very energetic environment in the proximity of the AGN (with a strong contribution to the $70\text{ }\mu\text{m}$ continuum), and a colder dust component farther out in the outer regions of the AGN torus and/or the host galaxy (the primary contribution to the $160\text{ }\mu\text{m}$ continuum).

We thank the referee for very useful comments that improved the paper. We would also like to acknowledge Dr. Ranjan Vasudevan for valuable comments on the work. We gratefully acknowledge support from NASA through Herschel contracts 1436909 (R.F.M., M.M., T.T.S.), 1427288 (A.J.B.), and 1447980 (L.L.C.). PACS has been developed by a consortium of institutes led by MPE (Germany) and including UVIE (Austria); KU Leuven, CSL, IMEC (Belgium); CEA, LAM (France); MPIA (Germany); INAF-IFSI/OAA/OAP/OAT, LENS, SISSA (Italy); IAC (Spain). This development has

been supported by the funding agencies BMVIT (Austria), ESA-PRODEX (Belgium), CEA/CNES (France), DLR (Germany), ASI/INAF (Italy), and CICYT/MCYT (Spain). The Herschel spacecraft was designed, built, tested, and launched under a contract to ESA managed by the Herschel/Planck Project team by an industrial consortium under the overall responsibility of the prime contractor Thales Alenia Space (Cannes), and including Astrium (Friedrichshafen) responsible for the payload module and for system testing at spacecraft level, Thales Alenia Space (Turin) responsible for the service module, and Astrium (Toulouse) responsible for the telescope, with in excess of a hundred subcontractors. This publication makes use of data products from the Wide-field Infrared Survey Explorer, which is a joint project of the University of California, Los Angeles, and the Jet Propulsion Laboratory/California Institute of Technology, funded by the National Aeronautics and Space Administration. The Cornell Atlas of Spitzer/IRS Sources (CASSIS) is a product of the Infrared Science Center at Cornell University, supported by NASA and JPL. This research has made use of NASA’s Astrophysics Data System. This research has made use of the NASA/IPAC Extragalactic Database (NED) which is operated by the Jet Propulsion Laboratory, California Institute of Technology, under contract with the National Aeronautics and Space Administration.

A. *Herschel PACS images*

Figure 10 shows the PACS *Scanamorphos* images for the BAT sample. The images are displayed with an inverse hyperbolic sine scaling (Lupton et al. 1999). All the images are presented in their native resolution and pixel size, 1.4 and $2.85''/\text{pixel}$ at 70 and $160\mu\text{m}$, respectively. The beam size at each wavelength is indicated by a black filled circle at the bottom left of each panel. The angular size of each panel is $2.2' \times 2.2'$. North is up, and East is left for all the images. Figures 10.11.105 are available in the online version of the Journal.

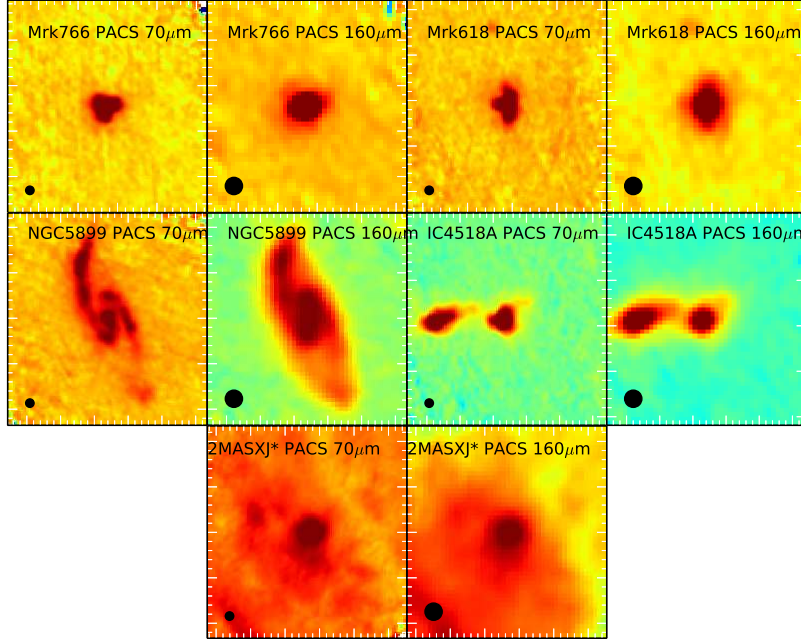


Fig. 10.— PACS images for different types of morphologies for the BAT sample. The images were randomly selected to show an example of a point-like source (Mrk 766), a slightly extended source (Mrk 618), a fully resolved source with complex structures (NGC 5899), a dual system (IC4518 pair) and a source contaminated from Galactic cirrus (2MASXJ20183871+4041003). The images are displayed with an inverse hyperbolic sine scaling (Lupton et al. 1999). All the *Scanamorphos* images are presented in their native resolution and pixel size, 1.4 and 2.85''/pixel at 70 and 160 μ m, respectively. The beam size at each wavelength is indicated by a black filled circle at the bottom left of each panel. The angular size of each panel is 2.2' \times 2.2'. North is up, and East is left for all the images. All the PACS images for the BAT sample are available in electronic form in the on-line version.

REFERENCES

- Akritas, M. G., & Siebert, J. 1996, MNRAS, 278, 919
- Antonucci, R. 1993, ARA&A, 31, 473
- Barger, A. J., Cowie, L. L., Mushotzky, R. F., Yang, Y., Wang, W.-H., Steffen, A. T., & Capak, P. 2005, AJ, 129, 578
- Bassani, L., Dadina, M., Maiolino, R., Salvati, M., Risaliti, G., della Ceca, R., Matt, G., & Zamorani, G. 1999, ApJS, 121, 473
- Bassani, L., Molina, M., Malizia, A., Panessa, F., Landi, R., Bazzano, A., Ubertini, P., Bird, A. J., & Stephen, J. B. 2013, ArXiv e-prints
- Baumgartner, W. H., Tueller, J., Markwardt, C. B., Skinner, G. K., Barthelmy, S., Mushotzky, R. F., Evans, P. A., & Gehrels, N. 2013, ApJS, 207, 19
- Beckert, T., & Duschl, W. J. 2004, A&A, 426, 445
- Bevington, P. R., & Robinson, D. K. 2003, Data reduction and error analysis for the physical sciences
- Bianchi, S., Miniutti, G., Fabian, A. C., & Iwasawa, K. 2005, MNRAS, 360, 380
- Burlon, D., Ajello, M., Greiner, J., Comastri, A., Merloni, A., & Gehrels, N. 2011, ApJ, 728, 58
- Calzetti, D., Wu, S.-Y., Hong, S., Kennicutt, R. C., Lee, J. C., Dale, D. A., Engelbracht, C. W., van Zee, L., Draine, B. T., Hao, C.-N., Gordon, K. D., Moustakas, J., Murphy, E. J., Regan, M., Begum, A., Block, M., Dalcanton, J., Funes, J., Gil de Paz, A., Johnson, B., Sakai, S., Skillman, E., Walter, F., Weisz, D., Williams, B., & Wu, Y. 2010, ApJ, 714, 1256

Casey, C. M. 2012, MNRAS, 425, 3094

Comastri, A., Iwasawa, K., Gilli, R., Vignali, C., Ranalli, P., Matt, G., & Fiore, F. 2010, ApJ, 717, 787

Cowie, L. L., Barger, A. J., Bautz, M. W., Brandt, W. N., & Garmire, G. P. 2003, ApJ, 584, L57

Dale, D. A., Aniano, G., Engelbracht, C. W., Hinz, J. L., Krause, O., Montiel, E. J., Roussel, H., Appleton, P. N., Armus, L., Beirão, P., Bolatto, A. D., Brandl, B. R., Calzetti, D., Crocker, A. F., Croxall, K. V., Draine, B. T., Galametz, M., Gordon, K. D., Groves, B. A., Hao, C.-N., Helou, G., Hunt, L. K., Johnson, B. D., Kennicutt, R. C., Koda, J., Leroy, A. K., Li, Y., Meidt, S. E., Miller, A. E., Murphy, E. J., Rahman, N., Rix, H.-W., Sandstrom, K. M., Sauvage, M., Schinnerer, E., Skibba, R. A., Smith, J.-D. T., Tabatabaei, F. S., Walter, F., Wilson, C. D., Wolfire, M. G., & Zibetti, S. 2012, ApJ, 745, 95

Dale, D. A., & Helou, G. 2002, ApJ, 576, 159

Dale, D. A., Helou, G., Contursi, A., Silbermann, N. A., & Kolhatkar, S. 2001, ApJ, 549, 215

D'Elia, V., Perri, M., Puccetti, S., Capalbi, M., Giommi, P., Burrows, D. N., Campana, S., Tagliaferri, G., Cusumano, G., Evans, P., Gehrels, N., Kennea, J., Moretti, A., Nousek, J. A., Osborne, J. P., Romano, P., & Stratta, G. 2013, A&A, 551, A142

Draine, B. T., & Li, A. 2007, ApJ, 657, 810

Elitzur, M., & Shlosman, I. 2006, ApJ, 648, L101

Fritz, J., Franceschini, A., & Hatziminaoglou, E. 2006, MNRAS, 366, 767

- Gandhi, P., Horst, H., Smette, A., Höning, S., Comastri, A., Gilli, R., Vignali, C., & Duschl, W. 2009, A&A, 502, 457
- Gordon, K. D., Engelbracht, C. W., Rieke, G. H., Misselt, K. A., Smith, J.-D. T., & Kennicutt, Jr., R. C. 2008, ApJ, 682, 336
- Hasinger, G., Miyaji, T., & Schmidt, M. 2005, A&A, 441, 417
- Helou, G., & Walker, D. W., eds. 1988, Infrared astronomical satellite (IRAS) catalogs and atlases. Volume 7: The small scale structure catalog, Vol. 7
- Höning, S. F., Gandhi, P., Asmus, D., Mushotzky, R. F., Antonucci, R., Ueda, Y., & Ichikawa, K. 2014, MNRAS, 438, 647
- Höning, S. F., & Kishimoto, M. 2010, A&A, 523, A27
- Ichikawa, K., Ueda, Y., Terashima, Y., Oyabu, S., Gandhi, P., Matsuta, K., & Nakagawa, T. 2012, ApJ, 754, 45
- Ikeda, S., Awaki, H., & Terashima, Y. 2009, ApJ, 692, 608
- Isobe, T., Feigelson, E. D., Akritas, M. G., & Babu, G. J. 1990, ApJ, 364, 104
- Isobe, T., Feigelson, E. D., & Nelson, P. I. 1986, ApJ, 306, 490
- Kaplan, E. L., & Meier, P. 1958, Journal of the American Statistical Association, 53, 457
- Kennicutt, R. C., & Evans, N. J. 2012, ARA&A, 50, 531
- Kennicutt, Jr., R. C. 1998, ARA&A, 36, 189
- Kennicutt, Jr., R. C., Armus, L., Bendo, G., Calzetti, D., Dale, D. A., Draine, B. T., Engelbracht, C. W., Gordon, K. D., Grauer, A. D., Helou, G., Hollenbach, D. J., Jarrett, T. H., Kewley, L. J., Leitherer, C., Li, A., Malhotra, S., Regan, M. W.,

- Rieke, G. H., Rieke, M. J., Roussel, H., Smith, J.-D. T., Thornley, M. D., & Walter, F. 2003, PASP, 115, 928
- Krolik, J. H., & Begelman, M. C. 1988, ApJ, 329, 702
- La Franca, F., Fiore, F., Comastri, A., Perola, G. C., Sacchi, N., Brusa, M., Cocchia, F., Feruglio, C., Matt, G., Vignali, C., Carangelo, N., Ciliegi, P., Lamastra, A., Maiolino, R., Mignoli, M., Molendi, S., & Puccetti, S. 2005, ApJ, 635, 864
- Lavalle, M., Isobe, T., & Feigelson, E. 1992, in Astronomical Society of the Pacific Conference Series, Vol. 25, Astronomical Data Analysis Software and Systems I, ed. D. M. Worrall, C. Biemesderfer, & J. Barnes, 245
- Lawrence, A. 1991, MNRAS, 252, 586
- Lebouteiller, V., Barry, D. J., Spoon, H. W. W., Bernard-Salas, J., Sloan, G. C., Houck, J. R., & Weedman, D. W. 2011, ApJS, 196, 8
- Lupton, R. H., Gunn, J. E., & Szalay, A. S. 1999, AJ, 118, 1406
- Madden, S. C., Rémy-Ruyer, A., Galametz, M., Cormier, D., Lebouteiller, V., Galliano, F., Hony, S., Bendo, G. J., Smith, M. W. L., Pohlen, M., Roussel, H., Sauvage, M., Wu, R., Sturm, E., Poglitsch, A., Contursi, A., Doublier, V., Baes, M., Barlow, M. J., Boselli, A., Boquien, M., Carlson, L. R., Ciesla, L., Cooray, A., Cortese, L., de Looze, I., Irwin, J. A., Isaak, K., Kamenetzky, J., Karczewski, O. Ł., Lu, N., MacHattie, J. A., O’Halloran, B., Parkin, T. J., Rangwala, N., Schirm, M. R. P., Schulz, B., Spinoglio, L., Vaccari, M., Wilson, C. D., & Wozniak, H. 2013, PASP, 125, 600
- Maiolino, R., Salvati, M., Bassani, L., Dadina, M., della Ceca, R., Matt, G., Risaliti, G., & Zamorani, G. 1998, A&A, 338, 781

- Malizia, A., Bassani, L., Panessa, F., de Rosa, A., & Bird, A. J. 2009, MNRAS, 394, L121
- Matsuta, K., Gandhi, P., Dotani, T., Nakagawa, T., Isobe, N., Ueda, Y., Ichikawa, K., Terashima, Y., Oyabu, S., Yamamura, I., & Stawarz, Ł. 2012, ApJ, 753, 104
- Meléndez, M., Kraemer, S. B., Armentrout, B. K., Deo, R. P., Crenshaw, D. M., Schmitt, H. R., Mushotzky, R. F., Tueller, J., Markwardt, C. B., & Winter, L. 2008a, ApJ, 682, 94
- Meléndez, M., Kraemer, S. B., Schmitt, H. R., Crenshaw, D. M., Deo, R. P., Mushotzky, R. F., & Bruhweiler, F. C. 2008b, ApJ, 689, 95
- Mor, R., Netzer, H., & Elitzur, M. 2009, ApJ, 705, 298
- Moshir, M., Kopan, G., Conrow, T., McCallon, H., Hacking, P., Gregorich, D., Rohrbach, G., Melnyk, M., Rice, W., Fullmer, L., White, J., & Chester, T. 1990, in Bulletin of the American Astronomical Society, Vol. 22, Bulletin of the American Astronomical Society, 1325
- Moustakas, J., Kennicutt, Jr., R. C., Tremonti, C. A., Dale, D. A., Smith, J.-D. T., & Calzetti, D. 2010, ApJS, 190, 233
- Mullaney, J. R., Alexander, D. M., Goulding, A. D., & Hickox, R. C. 2011, MNRAS, 414, 1082
- Murakami, H., Baba, H., Barthel, P., Clements, D. L., Cohen, M., Doi, Y., Enya, K., Figueredo, E., Fujishiro, N., Fujiwara, H., Fujiwara, M., Garcia-Lario, P., Goto, T., Hasegawa, S., Hibi, Y., Hirao, T., Hiromoto, N., Hong, S. S., Imai, K., Ishigaki, M., Ishiguro, M., Ishihara, D., Ita, Y., Jeong, W.-S., Jeong, K. S., Kaneda, H., Kataza, H., Kawada, M., Kawai, T., Kawamura, A., Kessler, M. F., Kester, D., Kii, T., Kim, D. C., Kim, W., Kobayashi, H., Koo, B. C., Kwon, S. M., Lee, H. M., Lorente,

- R., Makiuti, S., Matsuhara, H., Matsumoto, T., Matsuo, H., Matsuura, S., Müller, T. G., Murakami, N., Nagata, H., Nakagawa, T., Naoi, T., Narita, M., Noda, M., Oh, S. H., Ohnishi, A., Ohyama, Y., Okada, Y., Okuda, H., Oliver, S., Onaka, T., Ootsubo, T., Oyabu, S., Pak, S., Park, Y.-S., Pearson, C. P., Rowan-Robinson, M., Saito, T., Sakon, I., Salama, A., Sato, S., Savage, R. S., Serjeant, S., Shibai, H., Shirahata, M., Sohn, J., Suzuki, T., Takagi, T., Takahashi, H., Tanabé, T., Takeuchi, T. T., Takita, S., Thomson, M., Uemizu, K., Ueno, M., Usui, F., Verdugo, E., Wada, T., Wang, L., Watabe, T., Watarai, H., White, G. J., Yamamura, I., Yamauchi, C., & Yasuda, A. 2007, PASJ, 59, 369
- Murphy, K. D., & Yaqoob, T. 2009, MNRAS, 397, 1549
- Mushotzky, R. F., Shimizu, T. T., Meléndez, M., & Koss, M. 2014, ApJ, 781, L34
- Nenkova, M., Sirocky, M. M., Ivezić, Ž., & Elitzur, M. 2008a, ApJ, 685, 147
- Nenkova, M., Sirocky, M. M., Nikutta, R., Ivezić, Ž., & Elitzur, M. 2008b, ApJ, 685, 160
- Netzer, H. 2009, MNRAS, 399, 1907
- Neugebauer, G., Habing, H. J., van Duinen, R., Aumann, H. H., Baud, B., Beichman, C. A., Beintema, D. A., Boggess, N., Clegg, P. E., de Jong, T., Emerson, J. P., Gautier, T. N., Gillett, F. C., Harris, S., Hauser, M. G., Houck, J. R., Jennings, R. E., Low, F. J., Marsden, P. L., Miley, G., Olmon, F. M., Pottasch, S. R., Raimond, E., Rowan-Robinson, M., Soifer, B. T., Walker, R. G., Wesselius, P. R., & Young, E. 1984, ApJ, 278, L1
- Ott, S. 2010, in Astronomical Society of the Pacific Conference Series, Vol. 434, Astronomical Data Analysis Software and Systems XIX, ed. Y. Mizumoto, K.-I. Morita, & M. Ohishi, 139

- Pilbratt, G. L., Riedinger, J. R., Passvogel, T., Crone, G., Doyle, D., Gageur, U., Heras, A. M., Jewell, C., Metcalfe, L., Ott, S., & Schmidt, M. 2010, A&A, 518, L1
- Planck Collaboration, Ade, P. A. R., Aghanim, N., Arnaud, M., Ashdown, M., Aumont, J., Baccigalupi, C., Baker, M., Balbi, A., Banday, A. J., & et al. 2011, A&A, 536, A1
- Poglitsch, A., Waelkens, C., Geis, N., Feuchtgruber, H., Vandenbussche, B., Rodriguez, L., Krause, O., Renotte, E., van Hoof, C., Saraceno, P., Cepa, J., Kerschbaum, F., Agnèse, P., Ali, B., Altieri, B., Andreani, P., Augueres, J.-L., Balog, Z., Barl, L., Bauer, O. H., Belbachir, N., Benedettini, M., Billot, N., Boulade, O., Bischof, H., Blommaert, J., Callut, E., Cara, C., Cerulli, R., Cesarsky, D., Contursi, A., Creten, Y., De Meester, W., Doublier, V., Doumayrou, E., Duband, L., Exter, K., Genzel, R., Gillis, J.-M., Grözinger, U., Henning, T., Herreros, J., Huygen, R., Inguscio, M., Jakob, G., Jamar, C., Jean, C., de Jong, J., Katterloher, R., Kiss, C., Klaas, U., Lemke, D., Lutz, D., Madden, S., Marquet, B., Martignac, J., Mazy, A., Merken, P., Montfort, F., Morbidelli, L., Müller, T., Nielbock, M., Okumura, K., Orfei, R., Ottensamer, R., Pezzuto, S., Popesso, P., Putzeys, J., Regibo, S., Reveret, V., Royer, P., Sauvage, M., Schreiber, J., Stegmaier, J., Schmitt, D., Schubert, J., Sturm, E., Thiel, M., Tofani, G., Vavrek, R., Wetzstein, M., Wieprecht, E., & Wiezorrek, E. 2010, A&A, 518, L2
- Press, W. H., Teukolsky, S. A., Vetterling, W. T., & Flannery, B. P. 1992, Numerical recipes in FORTRAN. The art of scientific computing
- Rémy-Ruyer, A., Madden, S. C., Galliano, F., Hony, S., Sauvage, M., Bendo, G. J., Roussel, H., Pohlen, M., Smith, M. W. L., Galametz, M., Cormier, D., Lebouteiller, V., Wu, R., Baes, M., Barlow, M. J., Boquien, M., Boselli, A., Ciesla, L., De Looze, I., Karczewski, O. L., Panuzzo, P., Spinoglio, L., Vaccari, M., & Wilson, C. D. 2013, A&A, 557, A95

- Rice, W., Lonsdale, C. J., Soifer, B. T., Neugebauer, G., Kopan, E. L., Lloyd, L. A., de Jong, T., & Habing, H. J. 1988, ApJS, 68, 91
- Risaliti, G., Braito, V., Laparola, V., Bianchi, S., Elvis, M., Fabbiano, G., Maiolino, R., Matt, G., Reeves, J., Salvati, M., & Wang, J. 2009, ApJ, 705, L1
- Rosario, D. J., Santini, P., Lutz, D., Shao, L., Maiolino, R., Alexander, D. M., Altieri, B., Andreani, P., Aussel, H., Bauer, F. E., Berta, S., Bongiovanni, A., Brandt, W. N., Brusa, M., Cepa, J., Cimatti, A., Cox, T. J., Daddi, E., Elbaz, D., Fontana, A., Förster Schreiber, N. M., Genzel, R., Grazian, A., Le Floch, E., Magnelli, B., Mainieri, V., Netzer, H., Nordon, R., Pérez Garcia, I., Poglitsch, A., Popesso, P., Pozzi, F., Riguccini, L., Rodighiero, G., Salvato, M., Sanchez-Portal, M., Sturm, E., Tacconi, L. J., Valtchanov, I., & Wuyts, S. 2012, A&A, 545, A45
- Roussel, H. 2013, PASP, 125, 1126
- Sales, D. A., Ruschel-Dutra, D., Pastoriza, M. G., Riffel, R., & Winge, C. 2014, MNRAS, 441, 630
- Schartmann, M., Meisenheimer, K., Camenzind, M., Wolf, S., Tristram, K. R. W., & Henning, T. 2008, A&A, 482, 67
- Severgnini, P., Caccianiga, A., Della Ceca, R., Braito, V., Vignali, C., La Parola, V., & Moretti, A. 2011, A&A, 525, A38
- Skrutskie, M. F., Cutri, R. M., Stiening, R., Weinberg, M. D., Schneider, S., Carpenter, J. M., Beichman, C., Capps, R., Chester, T., Elias, J., Huchra, J., Liebert, J., Lonsdale, C., Monet, D. G., Price, S., Seitzer, P., Jarrett, T., Kirkpatrick, J. D., Gizis, J. E., Howard, E., Evans, T., Fowler, J., Fullmer, L., Hurt, R., Light, R., Kopan, E. L., Marsh, K. A., McCallon, H. L., Tam, R., Van Dyk, S., & Wheelock, S. 2006, AJ, 131, 1163

- Stalevski, M., Fritz, J., Baes, M., Nakos, T., & Popović, L. Č. 2012, MNRAS, 420, 2756
- Steffen, A. T., Barger, A. J., Cowie, L. L., Mushotzky, R. F., & Yang, Y. 2003, ApJ, 596, L23
- Tueller, J., Mushotzky, R. F., Barthelmy, S., Cannizzo, J. K., Gehrels, N., Markwardt, C. B., Skinner, G. K., & Winter, L. M. 2008, ApJ, 681, 113
- Tully, R. B. 1988, Nearby galaxies catalog
- Tully, R. B., Rizzi, L., Shaya, E. J., Courtois, H. M., Makarov, D. I., & Jacobs, B. A. 2009, AJ, 138, 323
- Ueda, Y., Akiyama, M., Ohta, K., & Miyaji, T. 2003, ApJ, 598, 886
- Ueda, Y., Eguchi, S., Terashima, Y., Mushotzky, R., Tueller, J., Markwardt, C., Gehrels, N., Hashimoto, Y., & Potter, S. 2007, ApJ, 664, L79
- Vasudevan, R. V., Brandt, W. N., Mushotzky, R. F., Winter, L. M., Baumgartner, W. H., Shimizu, T. T., Schneider, D. P., & Nousek, J. 2013, ApJ, 763, 111
- Véron-Cetty, M.-P., & Véron, P. 2010, A&A, 518, A10
- Vignali, C., & Comastri, A. 2002, A&A, 381, 834
- Weaver, K. A., Meléndez, M., Mushotzky, R. F., Kraemer, S., Engle, K., Malumuth, E., Tueller, J., Markwardt, C., Berghea, C. T., Dudik, R. P., Winter, L. M., & Armus, L. 2010, ApJ, 716, 1151
- Werner, M. W., Roellig, T. L., Low, F. J., Rieke, G. H., Rieke, M., Hoffmann, W. F., Young, E., Houck, J. R., Brandl, B., Fazio, G. G., Hora, J. L., Gehrz, R. D., Helou, G., Soifer, B. T., Stauffer, J., Keene, J., Eisenhardt, P., Gallagher, D., Gautier,

T. N., Irace, W., Lawrence, C. R., Simmons, L., Van Cleve, J. E., Jura, M., Wright, E. L., & Cruikshank, D. P. 2004, ApJS, 154, 1

Winter, L. M., Lewis, K. T., Koss, M., Veilleux, S., Keeney, B., & Mushotzky, R. F. 2010, ApJ, 710, 503

Winter, L. M., Mushotzky, R. F., Reynolds, C. S., & Tueller, J. 2009, ApJ, 690, 1322

Winter, L. M., Mushotzky, R. F., Tueller, J., & Markwardt, C. 2008, ApJ, 674, 686

Winter, L. M., Veilleux, S., McKernan, B., & Kallman, T. R. 2012, ApJ, 745, 107

Wright, E. L., Eisenhardt, P. R. M., Mainzer, A. K., Ressler, M. E., Cutri, R. M., Jarrett, T., Kirkpatrick, J. D., Padgett, D., McMillan, R. S., Skrutskie, M., Stanford, S. A., Cohen, M., Walker, R. G., Mather, J. C., Leisawitz, D., Gautier, III, T. N., McLean, I., Benford, D., Lonsdale, C. J., Blain, A., Mendez, B., Irace, W. R., Duval, V., Liu, F., Royer, D., Heinrichsen, I., Howard, J., Shannon, M., Kendall, M., Walsh, A. L., Larsen, M., Cardon, J. G., Schick, S., Schwalm, M., Abid, M., Fabinsky, B., Naes, L., & Tsai, C.-W. 2010, AJ, 140, 1868